NUMERICAL SIMULATIONS OF THE MAGNUS EFFECT IN BASEBALL AERODYNAMICS AND ROTATING CYLINDERS

by
John Scheffey

A thesis submitted to Johns Hopkins University in conformity with the requirements for the degree of Master of Science in Engineering

Baltimore, Maryland
December 2020

ABSTRACT

The motivation of the current study is to investigate the Magnus effect with numerical simulations to answer fundamental questions in two different applications: baseball aerodynamics and rotating cylinders, also known as Flettner rotors.

In baseball and many other ball sports, the Magnus effect – the movement of balls in flight due to their rotation – is fundamental to the strategy and competition of the game. However, the current understanding of the aerodynamics of baseball is incomplete, and many fundamental questions about the physics of baseball do not have clear answers – namely, what is the effect of the baseball seam on the flight of pitched and batted balls. In this study, the seam is investigated for its effect on flows past rotating spheres, along with the spin orientation and spin rate, to elucidate the seam's role in the flight of baseballs. A lateral "non-Magnus" force is found to exist depending on the ball's spin orientations and the height of the seam, leading to substantial deviations in the path of pitched baseballs. The implications of these findings for baseball competition are briefly discussed.

The second portion of this study explores modifications to Flettner rotors and considers their applications. First, active flow control via localized surface suction is simulated for three-dimensional cylinders and found to significantly enhance the aerodynamics performance of Flettner rotors. Second, rotating cylinders in shear flow with tapered profiles are simulated and compared to non-tapered cylinders, with a brief design study investigating their utility as a propulsion mechanism for a small unmanned aircraft.

Primary Reader and Advisor: Rajat Mittal

Secondary Reader: Jung-Hee Seo

TABLE OF CONTENTS

LIST OF FIGURES

CHAPTER 1. INTRODUCTION

The force generated on a rotating cylindrical body in cross flow is a widely observed phenomenon that is fundamental to many fluid dynamics applications. This effect has been observed and investigated by scientists as early as Isaac Newton, who noted the tendency of tennis balls to move along a curved path when struck with spin (Newton, 1671). Lord Rayleigh later attributed the first explanation of this effect to the Gustav Magnus; thus, the phenomenon became known as the *Magnus effect*. In general, this effect is understood to be caused by asymmetric boundary layer separation on rotating bodies. Boundary layer separation occurs further upstream on the side of the body moving against the flow, and further downstream on the side assisting the flow. The wake is then redirected towards the side of the body moving against the flow, yielding a deflection toward the opposite side. Common engineering applications of the Magnus effect include the spinning of guided missiles (Sturek et al., 1978), particle-laden flows in which small particles are often modeled as spheres (Wu et al., 2008; Liu & Prosperetti, 2010), as well as ships and aircraft that can leverage this force to generate thrust via spinning rotors (Seifert, 2012).

Perhaps the most readily observable occurrence of this phenomenon is in ball sports, including tennis, cricket, soccer, golf, and baseball, among other sports. In these sports, players can tactically manipulate the spin of balls to generate deflections in the ball's trajectory, producing a wide variety of outcomes. In tennis, players leverage "top spin" to generate a downwards force on the ball, enabling them to hit shots at higher velocities and making return shots more difficult for the opposition. In soccer, players may use "side spin" to generate a horizontal force, enabling the player to "curve" shots around defending players. In baseball, the Magnus effect is critical to both the pitching and hitting components of the game. Pitchers impart spin on a variety of types of pitches so as to create movement in different directions, such as the upward movement of a

"fastball", the downward movement of a "curveball", and the sideways movement of a "slider". Additionally, batters may attempt to hit balls with backspin so as to increase the distance a batted ball will travel. Mehta and Pallis (2002) conducted a review comparing the specific aerodynamics of strategic elements in a range of sports, focusing on the effects of velocity, spin, and surface roughness of spinning and non-spinning balls.

The boundary layer phenomenon is also understood to be relevant to the aerodynamics of sports balls, especially in the Reynolds number range of 40,000 to 400,000, at which most ball game are played (Mehta and Pallis, 2001). Smaller scale features on sports balls, such as the dimples on a golf ball, the seam on a baseball, or the patches on a soccer ball, are of the appropriate size to interact with the boundary layer in this Reynolds number range. This is especially apparent for non-spinning balls, sometimes called a "knuckleball", where boundary layer asymmetries caused by surface features can cause random, chaotic motion of balls, a phenomenon not observed in smooth balls without these features.

1.1 Baseball Aerodynamics

In the game of baseball, aerodynamics and the Magnus effect are central to the strategy and outcomes of the game, arguably more so than any other sport. From the inception of the game in the mid-19th century, pitchers readily discovered that manipulating the leather on the surface of the ball, the stitching around the ball, and the spin could impact the trajectory of the ball in flight. This led to the development of a wide variety of pitches, including the curveball, screwball, spitball, and knuckleball, which manipulate the trajectories of pitched balls in different fashions in an attempt to deceive batters (The Neyer/James Guide to Pitchers, 2004). This practice was not without controversy; in the early 1870s, upon learning that one of the pitchers on the Harvard

baseball team was throwing curveballs, university president Charles W. Eliot reportedly threatened to shut down the program, stating, "I have heard that this year we won the championship because we have a pitcher who has a fine curve ball. I am further instructed that the purpose of the curve ball is to deliberately deceive the batte. Harvard is not in the business of teaching deception." (Baseball, 1994) The "spitball" rose to prominence in the early-20th century, as pitchers discovered that saliva, Vaseline, mud, and many other "foreign substances" could be used to create asymmetries on the ball or allow it to "slip" out of the pitcher's hand with minimal spin, creating an effect similar to a "knuckleball". Eventually, the practice of "doctoring the baseball" was banned altogether by Major League Baseball in 1920. Although the practice of throwing curveballs had been around for several decades, there was still appreciable controversy over whether or not curving the path of the ball was physically possible, or a mere illusion. An experimental study published in the *American Journal of Physics* by Verwiebe (1942) concluded that balls "dropped more sharply than would be the case for free fall alone."

Briggs (1959) was among the first published works experimentally investigating and quantifying the aerodynamics of baseballs. In his study, Briggs tested the effect of spin rate and wind speed on the movement of baseball by dropping vertically spinning baseballs in a horizontal wind tunnel and measuring their lateral deflections. As shown in Fig 1-1, for fixed wind speeds, the lateral deflections were found to be approximately linear with spin rate.

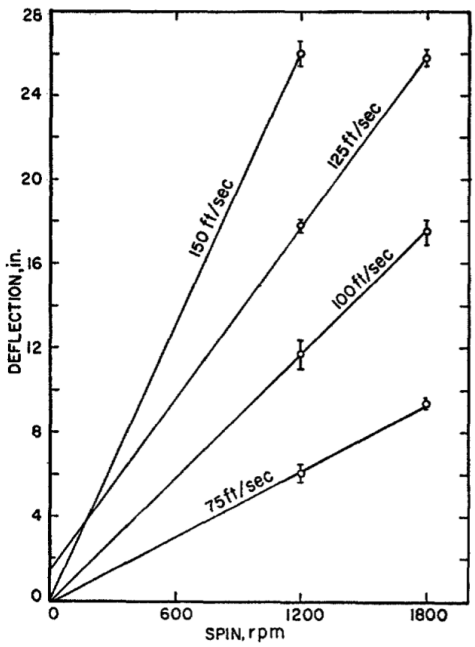

Figure 1-1. Lateral deflection of a vertically spinning baseball in a horizontal windstream, from Briggs (1959)

Watts and Sawyer (1975) performed investigations into the erratic motions of knuckleballs, or balls thrown with minimal spin. Significant fluctuations in the lateral force were observed depending on the orientation of the ball, concluding that the motion of knuckleballs is due to the very slow spin "changing the location of the roughness elements (strings), and thereby causing a nonsymmetric velocity distribution and a shifting of the wake." Nathan (2008) performed further experimental investigations into the Magnus force on a baseball, and the implications for the total flight distance of batted balls. The lift coefficient C_L was investigated for its dependence on the spin factor $S = \frac{R\omega}{v}$, where R is the ball radius, ω is the rotation rate, and v is the ball velocity. Fig 1-2(a) shows experimental determinations of C_L with varying S from several studies, as well as proposed parameterizations. C_L is found to be roughly linear with S, above a critical $S \approx 0.1$. Fig 1-2(b) shows the variation of C_L with v for values of S in the range of 0.15-0.25, which are common

to pitched baseballs. C_L was found to not strongly depend on v over the range 50-110 mph, or Re from $(1.1 - 2.4) \times 10^5$.

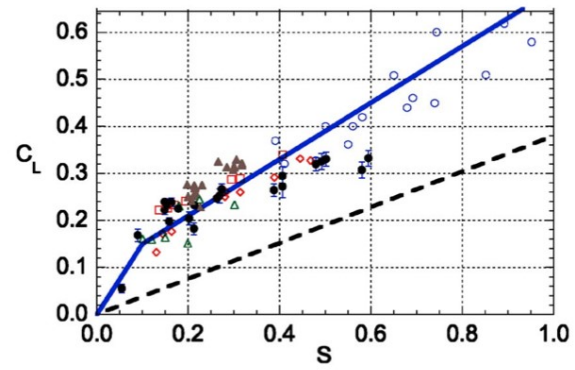

(a)

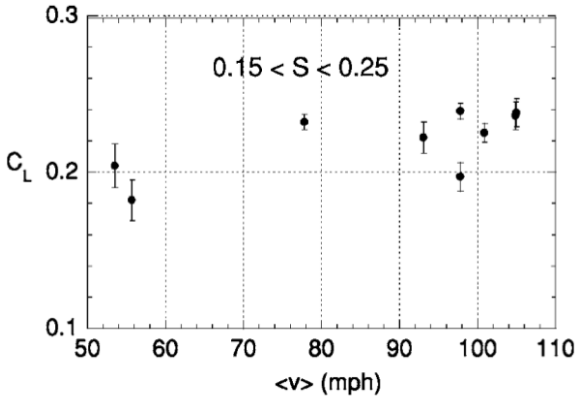

(b)

Figure 1-2. (a) Experimental values of C_L vs. spin parameter S, from Nathan (2008); (b) Experimental values of C_L vs. v for fixed $0.15 < S < 0.25$, from Nathan (2008)

In recent years, optical and radar technologies have enabled significant advances in the understanding of the trajectories of baseballs in flight. Since as early as 2006, Major League Baseball systems have been equipped with ball tracking systems which can measure pitched ball quantities such as velocity, movement, spin axis, and spin rate, along with batted ball quantities such as exit velocity and launch angle. This new ability to measure the motion of baseballs in situ

for tens of thousands of events has enabled physicists to further examine the validity of many assumptions about baseball aerodynamics – namely, that the motion of baseballs is solely attributable to the Magnus effect. While the Magnus effect is undoubtedly the dominant force affecting the trajectory of spinning balls, observers have noted instances where a "Magnus model" does not fully explain the movement of pitches.

Most of the early works on baseball aerodynamics (Briggs, 1959; Rex, 1985) conclude that for balls with sufficient spin, seam orientation does not significantly impact the trajectory; however, in cases where balls deviate from a Magnus model prediction, seam orientation is thought to potentially play an important role. Similar to the asymmetries observed by Watts and Ferrer (1975) for non-spinning balls, it is proposed that for spinning ball with certain seam orientations, the seam can be positioned in such a way to produce consistent boundary layer asymmetries to one side, resulting in lateral "non-Magnus" deflections. Smith and Smith (2020) leveraged particle image velocimetry (PIV), high-speed cameras, and optical pitch tracking technologies to experimentally investigate this effect. They find that seams positioned within a narrow range of orientations do indeed cause early (upstream) boundary layer separation to one side of the ball, leading to deflections perpendicular to the Magnus lift force, a phenomenon nicknamed the "Seam Shifted Wake".

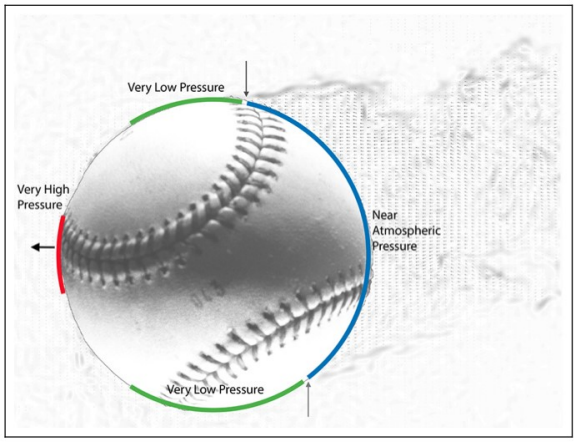

(a)

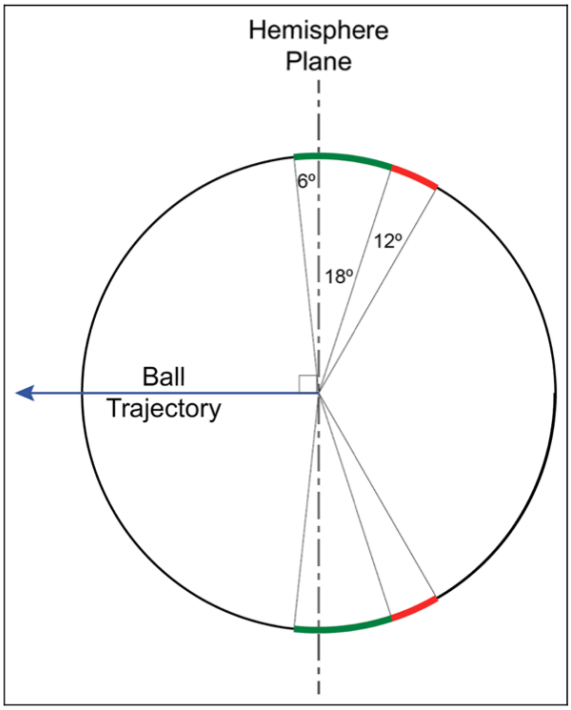

(b)

Figure 1-3. (a) PIV of leftward traveling baseball, with the seam the seam on the top side causing early boundary layer separation and deflecting the wake upward, from Smith and Smith (2020); (b) Proposed critical seam orientations relative to ball trajectory (green) compared to turbulent separation point with no seam present, from Smith and Smith (2020).

In addition to the "Seam Shifted Wake" effect, there are many other significant aspects of baseball aerodynamics still in question. The recent, dramatic surge in home run rates in Major League Baseball beginning around 2015 has drawn the attention of physicists, statisticians, and even casual fans interested in explaining large annual changes in baseball physics – with speculation that ball aerodynamic properties were intentionally modified by MLB so as to increase home run rates. A committee of scientists from various disciplines concluded that "…the aerodynamic properties (primarily the drag and lift coefficients) are a major contributing factor to the home run surge…" (Albert et al., 2018) Other current research topics include the effect of seam height and profile, the magnitude of spin "decay" throughout ball flight, and many others.

1.2 FLOWS PAST ROTATING SPHERES

In the broader fluid dynamics community, the flow past a sphere has been a key research topic for several decades, particularly because of the application to the transport of particles, which are commonly modeled as spheres. Rubinow and Keller (1961) investigated the Magnus lift force in the Stokes regime, deriving the expression $C_L = 2\omega^*$, where $\omega^* = \frac{\omega D}{2U_\infty}$ is the dimensionless rotation rate (also denoted as S or Ω^*). For Reynolds numbers ($Re = \frac{U_\infty D}{\nu}$) above the Stokes regime, extensive experimental testing has been done in the laminar, transitional, and turbulent regimes. One of the most extensively studied phenomena for flows past spheres is the drag crisis. Famously discovered by Eiffel (1912) in his laboratory in the Eiffel tower, the drag coefficient on a smooth sphere suddenly drops at $Re = 2 - 3 \times 10^5$. For spheres with surface roughness, the drag crisis occurs at lower Re, a discovery which explains the utility of dimples on a golf ball.

Transversely rotating spheres – where the sphere's axis of rotation is orthogonal to the free-stream direction - have been the subject of numerous investigations by fluid dynamicists due to

the Magnus effect induced by these flows and its many engineering applications. Direct numerical simulations (DNS) have greatly helped to quantify and characterize these flows at various Reynolds numbers and dimensionless rotation rates. For moderate Reynolds numbers ($Re = 100 - 300$), Kim (2009) and Giacobello et al. (2009) characterized different flow regimes and quantified force coefficients for $\Omega^* \leq 1.2$. The flow was found to be steady at $Re = 100$ for all rotation rates, transitioning from steady to unsteady for higher Re, depending on ω^*, with unsteady flows characterized in either "vortex shedding" or "shear layer instability" regimes. Poon et al. (2014) further investigated transverse rotating spheres at higher Re of $500 - 1000$, uncovering an additional "shear layer-stable foci" regime for high values of ω^*. Figure 1-4, below, shows a map of the various unsteady flow regimes depending on Re and ω^*.

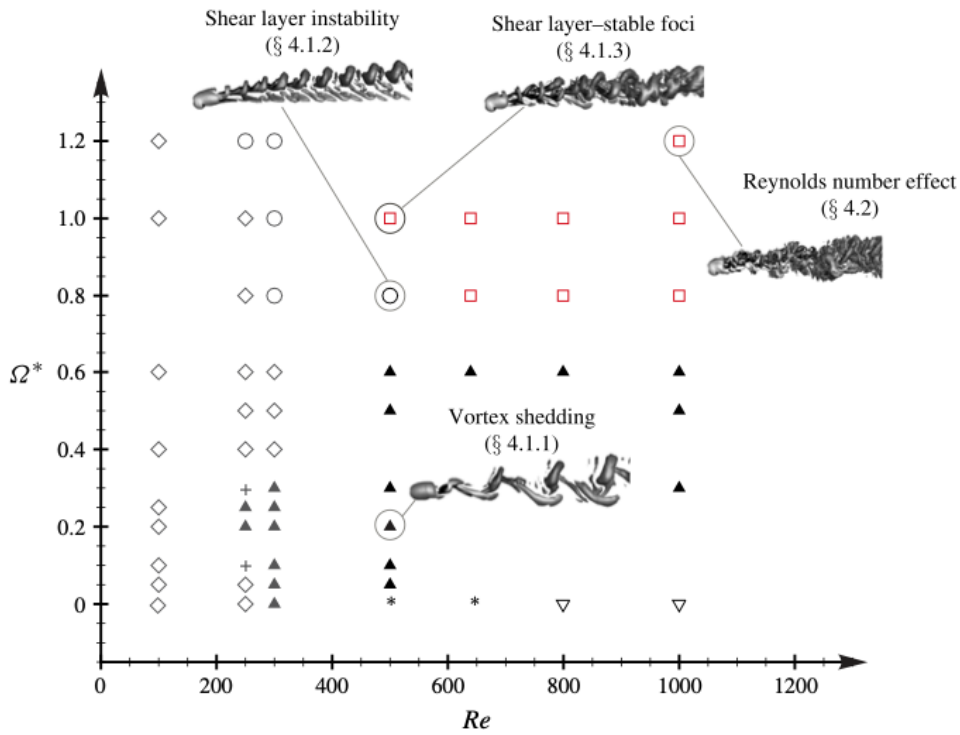

Figure 1-4. Different flow regimes for transversely rotating spheres, from Poon et al. (2014)

The flow regimes for streamwise rotating spheres – where the sphere's axis of rotation aligns with the free-stream direction – have been studied mostly experimentally (Luthander & Rydberg, 1935; Hoskin, 1955; Schlichting, 1979). Kim and Choi (2002) performed numerical simulations of these flows at $Re = 100, 250,$ and 300, varying ω^* from $0 - 1.0$. Time-averaged lift values were found to be zero for all $\omega^* > 0$, while the drag was found to increase monotonically with rotation speed. Poon et al. (2010) investigated the effect of changing the rotation axis α from streamwise rotation ($\alpha = 0$) to transverse rotation ($\alpha = \frac{\pi}{2}$) on laminar flow structures. Both C_L and C_D were found to increase monotonically with α for all Re, with the effect of α increasing with ω^*. At $Re = 100$, the flow was found to be steady and symmetric for all values of ω^*, while for $Re = 250$ and 300, the wakes are either steady or unsteady depending on α and ω^*, generally transitioning from helical, "frozen" threads at low α to planar symmetric flow at $\alpha = \frac{\pi}{2}$, either with steady vortex threads or unsteady "hairpin" vortex shedding depending on ω^*. While numerical studies have helped to illuminate the behavior of force coefficients and flow regimes with varying spin rates and rotation axes, there is still much left to investigate. Namely, there is a need for understanding of the flow behavior at higher Reynolds numbers in the transitional regime, as well as a more complete description of the effect of α by sampling more values between $0 - \frac{\pi}{2}$.

1.3 FLOWS PAST ROTATING CYLINDERS

The experiments conducted by Gustav Magnus (1853) were performed on rotating cylinders. The experimental setup (Fig 1-5) consisted of a brass cylinder on bearings mounted to two arms, with the arms mounted to a freely rotating post. After spinning the cylinder with a string and directing a wind towards the cylinder, he observed that the cylinder would always move

towards the side of the rotation assisting the flow; thus, this phenomenon was named the "Magnus effect".

Prandtl (1925) was among the first to quantify the Magnus effect for a rotating cylinder, where he proposed that the maximum lift for a spinning cylinder in a uniform flow is 4π. Prandtl also studied the end conditions of the cylinder and demonstrated that end plates and higher aspect ratios (L/D) could increase the maximum theoretical lift. Anton Flettner, observing that the Magnus effect in a cross-wind would yield a much greater thrust than a sail of equivalent size, attempted to use spinning rotors as a means of ship propulsion, a concept later confirmed in wind tunnel tests of cylinders with endplates. This type of rotor on ships became known as a "Flettner rotor" and has been used on vessels as an energy-saving means of propulsion. Another major application of the Magnus force for rotating cylinders is aircraft propulsion, such as in the PlymouthA-A-2004 (Figure 1-6). However, these "Flettner airplanes" have not seen been as widely used as Flettner rotors on ships.

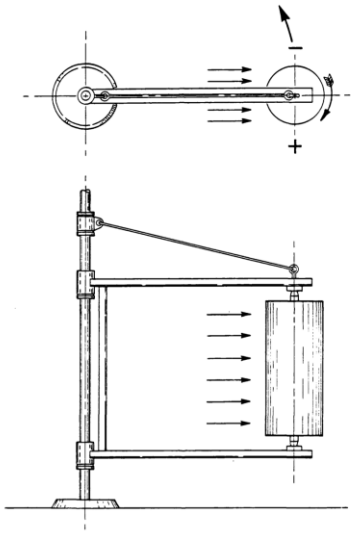

Figure 1-5. Gustav Magnus's experimental setup, conducted in 1853, from Borg (1986)

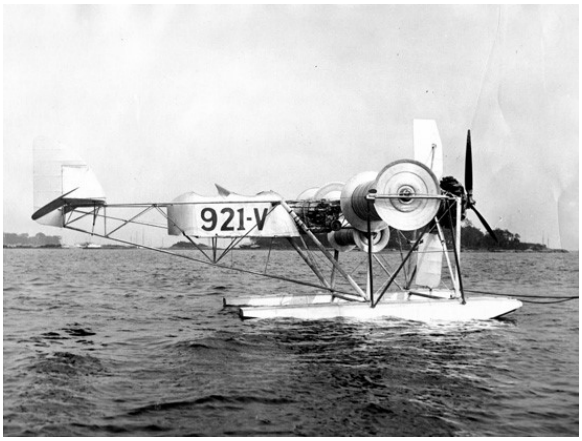

Figure 1-6. Plymouth A-A-2004 built in 1930 by anonymous inventors, from Deutches Museum - Archive

Many experimental and computational studies have been done on rotating cylinder and cylinders with end plates, mainly seeking to quantify the effect of Reynolds number and velocity ratio (also called spin parameter) on stability and force coefficients. In a recent review paper, Seifert (2012) summarized much of the current understanding of the Magnus effect for rotating cylinders. The main factor influencing these flows in the velocity ratio $\omega^* = \frac{\omega D}{2U_\infty}$ (also called α, not to be confused with the rotation axis α for a spinning sphere). For $0 \leq \omega^* \leq 1.9$ (Mittal and Kumar, 2003), a Kármán vortex street of periodic vortex shedding is observed, a behavior seen across a wide range of Re up to at least $Re = 8 \times 10^6$ (Zdravkovich, 1997). In Mittal and Kumar's (2003) study at $Re = 200$, the flow is found to be steady for $1.9 < \omega^* \leq 4.3$, becoming unsteady for $4.3 < \omega^* < 4.75$, and again becoming unsteady at higher ω^*. The onset of the second unsteady shedding regime is dependent on Re, with shedding occurring at lower ω^* for increased Re (Seifert, 2012).

Numerous studies have looked at extensions of a simple rotating circular cylinder, including adding end plates, introducing surface roughness, changing aspect ratios, introducing

intermediate disks along the span of the cylinder, and rounding the ends of the cylinder. Active flow control, via surface suction or blowing, has been examined as a way to modify flows and enhance aerodynamic performance. Two main applications for surface suction on cylinders have been investigated: uniform suction across the entire cylinder surface via a porous wall, and localized or "slot" suction, where only part of the cylinder surface has a suction element. Hurley and Thwaites (1951) demonstrated that sufficient uniform surface suction can reduce drag and suppress vortex shedding. Fransson et al. (2004) demonstrated that even moderate amount of suction ($\leq 5\%$ of the free-stream velocity) can delay separation and narrow the wake of rotating cylinders, thus reducing the drag. Recently, Ramsay et al. (2019) demonstrated that non-uniform suction can be substantially more effective than uniform suction at eliminating boundary layer separation. Studies have also examined the effect of non-uniform cylinder geometries on flows past predominantly stationary cylinders. Gaster (1969) conducted water tunnel experiments of flows past slender cones at taper ratios of 18:1 and 36:1, and further studies of flow behind stationary tapered cylinders in uniform flow have been done by Papangelou (1992) and Anderson & Szewczyk (1995). However, there appears to be little work thus far on rotating tapered cylinders.

CHAPTER 2. METHODS

This chapter details the numerical flow solver used to perform the experiments in this work, as well as the specific simulation details and study parameters for both baseball simulations and Flettner rotor simulations. The flow solver used for this study is ViCar3D, a sharp-interface immersed boundary method code developed by Dr. Rajat Mittal's research group (Mittal et al., 2008; Seo and Mittal, 2011). This solver is robust in its ability to simulate a wide range of internal and external flows using simple, non-conforming Cartesian grids. This approach is particularly useful for moving boundary cases such as a rotating ball with a seam, it avoids the need for moving or highly deformed grids which need to be recomputed throughout the simulation (Mittal & Iaccarino, 2005). The flow solver and immersed boundary method are not original to this work, but a brief overview is included for completeness.

2.1 VICAR3D FLOW SOLVER

The governing equations for flows past rotating bodies are the three-dimensional, incompressible Navier-Stokes equations with constant properties given by

$$\frac{\partial \mathrm{u_i}}{\partial x_i} = 0$$

$$\frac{\partial u_i}{\partial t} + \frac{\partial (u_i u_j)}{\partial x_j} = -\frac{1}{\rho}\frac{\partial \mathrm{p}}{\partial \mathrm{x_i}} + \nu \frac{\partial}{\partial x_j}\left(\frac{\partial u_i}{\partial x_j}\right)$$

where $i; j = 1,2,3$, u_i are the velocity components, p is the pressure, ρ is the fluid density, and ν is the fluid kinematic viscosity.

The Navier-Stokes equations are discretized on a Cartesian grid, with collocated storage of p and u_i at the cell centers, and U_i computed at face centers. Time integration of these equations is done using a three-step Van-Kan fractional step method (Van Kan, 1986). The first sub-step of

this method solves a modified momentum equation and obtains an intermediate velocity u^*. A second-order Adams-Bashforth scheme is used for the convection terms, with an implicit Crank-Nicolson scheme for the diffusion terms, thereby eliminating the viscous stability constraint. The modified momentum equation solved at the cell nodes is

$$\frac{u_i^* - u_i}{\Delta t} + \frac{1}{2}[3N_i^n - N_i^{n-1}] = -\frac{1}{\rho}\frac{\delta p^n}{\delta x_i} + \frac{1}{2}(D_i^* + D_i^n)$$

where $N_i = \frac{\partial(U_j u_i)}{\partial x_j}$ is the convective term and $D_i = \nu\left(\frac{\delta}{\delta x_j}\right)\left(\frac{\delta u_i}{\partial x_j}\right)$ is the diffusion term, with $\frac{\delta}{\delta x_i}$ denoting second-order central differencing. A second-order hybrid differencing scheme is used for the convective discretization. These equations are then solved with a line-SOR scheme (Anderson et al., 1984). Face center velocities U_i are then computed by averaging across adjacent cell center values in orthogonal directions. Similar to a fully staggered arrangement, only the face velocity component normal to the cell face is used for computing volume flux through each cell. The averaging procedure for computing face velocities is as follows:

$$\widetilde{u_\iota} = u_i^* + \Delta t \frac{1}{\rho}\left(\frac{\delta p^n}{\delta x_i^n}\right)_{cc}$$

$$\widetilde{U_1} = \gamma_W \widetilde{u_{1P}} + (1 - \gamma_W)\widetilde{u_{1W}}$$

$$\widetilde{U_2} = \gamma_S \widetilde{u_{2P}} + (1 - \gamma_S)\widetilde{u_{2S}}$$

$$\tilde{3} = \gamma_B \widetilde{u_{3P}} + (1 - \gamma_B)\widetilde{u_{3B}}$$

$$U_i^* = \widetilde{U_\iota} - \Delta t \frac{1}{\rho}\left(\frac{\delta p^n}{\delta x_i^n}\right)_{fc}$$

where γ_W, γ_S, and γ_B are linear interpolation weights for the west, south, and back face velocity components, respectively. The subscripts "fc" and "cc" denote cell-center and face-center gradients, respectively. Figure 2-1 depicts the naming conventions and locations of velocity components for the spatial discretization of a fluid cell.

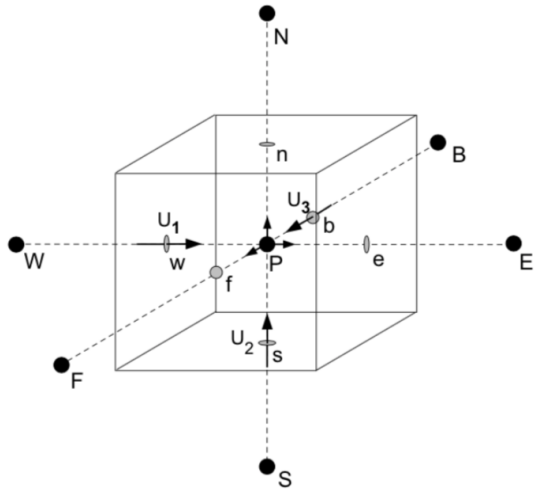

Figure 2-1. Naming conventions and positions of velocity components, from Mittal et al. (2008)

The second sub-step uses the intermediate velocities computed in the first step to solve the pressure correction equation

$$\frac{u_i^{n+1} - u_i^*}{\Delta t} = -\frac{1}{\rho}\frac{\delta p'}{\delta x_i}$$

which is solved with the condition that u_i^{n+1} is divergence free, to satisfy condition given in the mass equation. This leads to the following Poisson equation for the pressure correction,

$$\frac{1}{\rho}\frac{\delta}{\delta x_i}\left(\frac{\delta p'}{\delta x_i}\right) = \frac{1}{\Delta t}\frac{\delta U_i^*}{\delta x_i}$$

with a Neumann boundary condition for the pressure imposed on all boundaries.

To solve this pressure Poisson equation, a geometric multi-grid method is used (Bozkurttas et al., 2005) with a Gauss-Siedel line-SOR smoother (Zeigel et al., 1987). Because this solver utilizes non-conforming Cartesian grids, iterative solvers such as the geometric multi-grid method can be employed in a highly efficient manner with relatively little overhead memory requirements, a critical advantage over body-fitted, unstructured grids, which may require the use of less efficient or more complex multi-grid methods. Coupled with a Gauss-Siedel line-SOR smoother, this

geometric multi-grid method becomes highly efficient, nearly approaching the ideal theoretical performance in which the solution scales linearly with the number of grid points.

After solving the Poisson equation for the pressure, the velocity and pressure are updated in the final step as

$$p^{n+1} = p^n + p'$$

$$u_i^{n+1} = u_i^* - \Delta t \frac{1}{\rho}\left(\frac{\delta p'}{\delta x_i}\right)_{cc}$$

$$U_i^{n+1} = U_i^* - \Delta t \frac{1}{\rho}\left(\frac{\delta p'}{\delta x_i}\right)_{fc}$$

The separately updated face velocities satisfy discrete mass conservation to machine accuracy and are used for estimating the non-linear convective flux terms, which enforces geometric conservation for the convective flux. The concept of separately calculating face- and cell-center velocities was first introduced by Zang et al. (1994) and applied to Cartesian grid methods in Ye et al. (1999). This collocated scheme allows for simpler implementation compared to conventional staggered mesh schemes (Zang et al., 1994) and has good discrete kinetic energy properties (Felten and Lund, 2000), making it robust for relatively high Reynolds number flow with little to no artificial dissipation or upwinding.

2.2 IMMERSED BOUNDARY METHOD

The immersed boundary method uses a multi-dimensional ghost-cell methodology to impose boundary conditions on either stationary or moving immersed boundaries. The internal boundary is represented by an unstructured mesh of triangular elements, then immersed within the Cartesian grid. Grid cells are then identified based on their node position as being either inside the solid body (“solid cells”) or inside the fluid domain (“fluid cells”). Cells whose nodes are inside

the solid body but are adjacent to at least one fluid cell are identified as “ghost cells”. Once all cells are identified, an appropriate boundary condition on the ghost cells must then be enforced. This is done by first detecting the “image point” of all ghost cells by projecting a line from the ghost cell node through the boundary intercept such that the line is normal to the boundary and the boundary intercept lies at the midpoint of this line. A representative depiction of a 2D immersed boundary is shown in Figure 2-2.

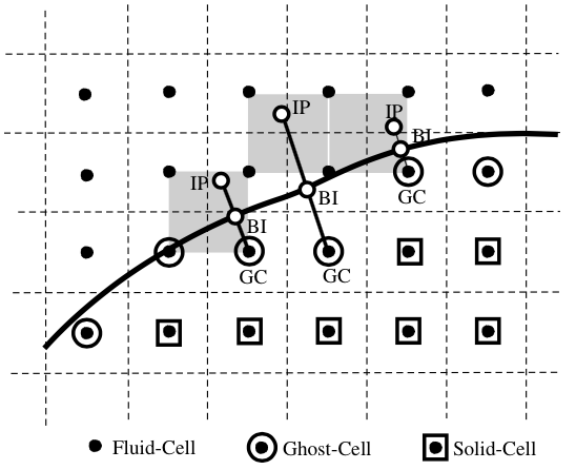

Figure 2-2. 2D schematic of example immersed boundary. “GC” denotes ghost cell nodes, “BI” denotes boundary intercept points, and “IP” denotes image points. (From Mittal et al., 2008)

With the boundary intercept and image point computed for each ghost cell, a trilinear interpolation is used to express the general variable ϕ in eight nodes surrounding the image point, with the following form:

$$\phi(x_1, x_2, x_3) = C_1 x_1 x_2 x_3 + C_2 x_1 x_2 + C_3 x_2 x_3 + C_4 x_1 x_3 + C_5 x_1 + C_6 x_2 + C_7 x_3 + C_8$$

The eight unknown coefficients, $\{C\}^T = \{C_1, C_2, \dots, C_8\}$, are determine by solving the inverse problem

$$\{C\} = [V]^{-1}\{\phi\}$$

Here, $[V]$ is the Vandermonde matrix (Press et al., 1992), which has the form

$$[V] = \begin{bmatrix} x_1x_2x_3|_1 & x_1x_2|_1 & x_1x_3|_1 & x_2x_3|_1 & x_1|_1 & x_2|_1 & x_3|_1 & 1 \\ x_1x_2x_3|_2 & x_1x_2|_2 & x_1x_3|_2 & x_2x_3|_2 & x_1|_2 & x_2|_2 & x_3|_2 & 1 \\ \vdots & \vdots & \vdots & \vdots & \vdots & \vdots & \vdots & \vdots \\ x_1x_2x_3|_8 & x_1x_2|_8 & x_1x_3|_8 & x_2x_3|_8 & x_1|_8 & x_2|_8 & x_3|_8 & 1 \end{bmatrix}$$

With subscripts $\{1,2,3,\dots,8\}$ denoting the index of the cells surrounding the image point. The quantities at the image point are then calculated as

$$\phi_{IP} = \sum_{i=1}^{8} \beta_i \phi_i + T.E.$$

Here, $\beta's$ are weights that depend on the coordinates of the image point and $\phi_i's$ are values at the neighboring cells.

With image point values determined, a central difference approximation is used along the line normal to the boundary intercept to implement Dirichlet and Neumann boundary conditions on the immersed boundary, with the following schemes

$$\phi_{GC} = 2\phi_{BI} - \phi_{IP}$$

$$\phi_{GC} = \Delta l_p \left(\frac{\partial \phi}{\partial n}\right)_{BI} + \phi_{IP}$$

where Δl_p is the length of the line segment between the ghost cell node and the image point. These can be rewritten in the following implicit form

$$\phi_{GC} + \sum_{i=1}^{8} \beta_i \phi_i = 2\phi_{BI}$$

$$\phi_{GC} - \sum_{i=1}^{8} \beta_i \phi_i = -\Delta l_p \left(\frac{\partial \phi}{\partial n}\right)_{BI}$$

These are solved with the governing equations to obtain the pressure and velocities. With this method, second-order accuracy in space and time is preserved both locally and globally (Mittal et al., 2008).

2.3 SIMULATION SETUP – BASEBALL AERODYNAMICS

A general schematic of the problem geometry and coordinates is shown in Figure 2-3. Note that the z-direction is the streamwise direction. The rotation axis is varied in the xz-plane.

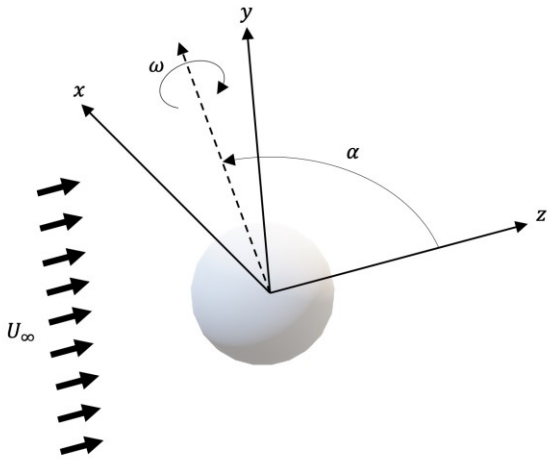

Figure 2-3. Problem schematic for rotating spheres and baseballs. The spin axis α is varied in the xz-plane, and measured from the $+z$-axis. The spin ω is positive from a right-hand rule convention.

Flows are solved on a structured Cartesian mesh with either a sphere or a baseball as the immersed boundary. The domain, boundary conditions, and simulation setup are kept identical between sphere and baseball simulations. A computational domain with size $13D \times 13D \times 25D$ is used, with D the diameter of the sphere. Figure 2-4 shows a 3D isometric view of the computational domain used.

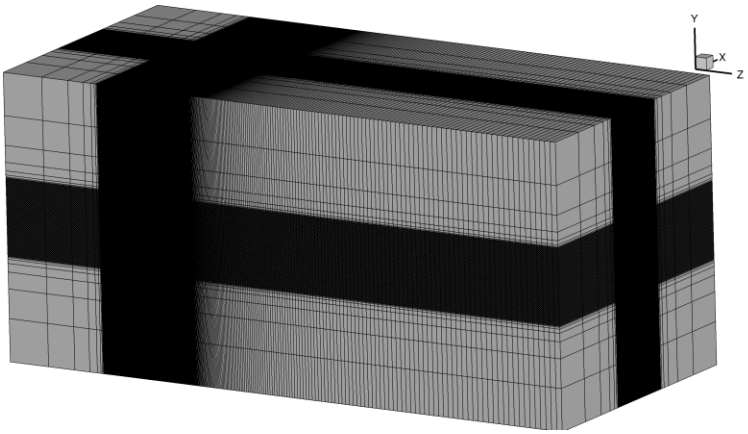

Figure 2-4. Computational domain used in simulations of rotating spheres/baseballs

The domain is comprised of 8.6 million cells, with 160 points in the *x*- and *y*-directions, and 336 points in the *z*-direction. Figure 2-5 shows a 2D cross-section of the computational domain in the *yz*-plane, through the center of the sphere. A fine-mesh region of size $3D \times 3D \times 4D$ is used near the sphere, with a uniform grid spacing $\Delta x = D/48$. In the upstream and streamwise directions, the grid is stretched rapidly away from the fine-mesh region. Downstream of the sphere, the grid is slowly stretched using a hyperbolic tangent stretching function, maintaining a stretching ratio $\frac{\Delta x_{i+1}}{\Delta x_i} \approx 2.6\%$. Due to the "downward" deflection of the wake expected with the rotation of the sphere, the sphere is placed in the "upper-left" corner of the fine-mesh region, or $0.25D$ from the boundary of the fine-mesh region in both the *y*- and *z*-directions. The sphere is kept centered in the *x*-direction due to the expected symmetry about the *yz*-plane for transverse rotating spheres. Note that in the case of streamwise rotation, a "downward" deflection of the wake is no longer expected so the sphere is kept centered in the *y*-direction.

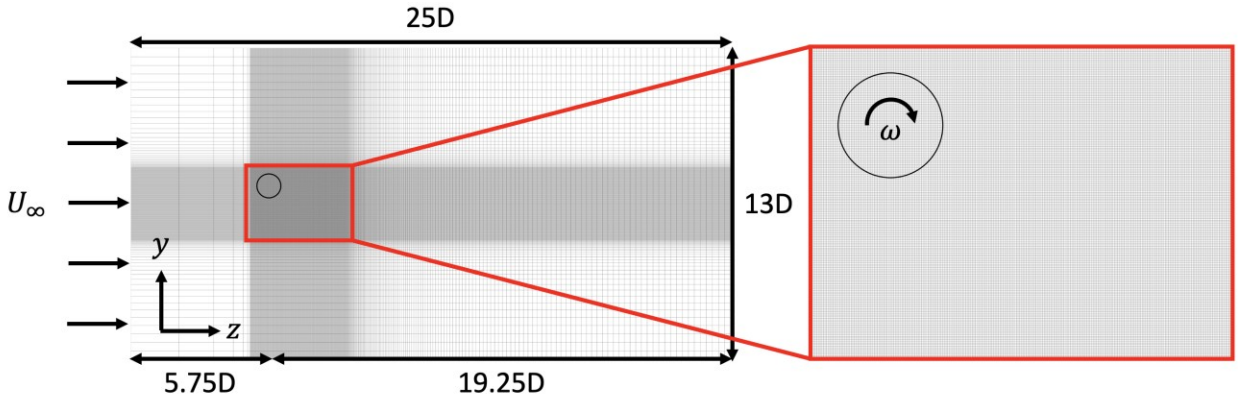

Figure 2-5. 2D view (*yz*-plane) of overall computational domain (left) with inset (right) of fine mesh region near the sphere

At the inlet ($z = 0$) as well as all side-walls, a Dirichlet boundary condition is imposed on the velocity, with $\boldsymbol{u} = (0,0,U_\infty)$. A zero-gradient Neumann boundary condition is imposed on the velocity at the outlet ($z = 25D$). On the internal boundary, no-slip and no-penetration boundary conditions are imposed.

While generating a sphere as an internal boundary is trivial, simulations of baseballs require external mesh generation. To best simulate actual baseball aerodynamics, a SolidWorks model of a baseball is first generated to the approximate geometry of a Major League Baseball (MLB) ball (Albert et al., 2018) (Figure 2-6a). While ideally the exact topography of an in-game MLB ball would be used, there are many secondary, small-scale features including gaps between individual stitches, stitching holes, and small irregularities that cannot reasonably be resolved by a numerical code. Because of this, the baseball model used in these simulations is somewhat simplified and smoothened to retain the first-order features of the baseball seam, namely the helical, winding path around the sphere, and the "bump" cross-sectional profile of the seam (Figure 2-6b).

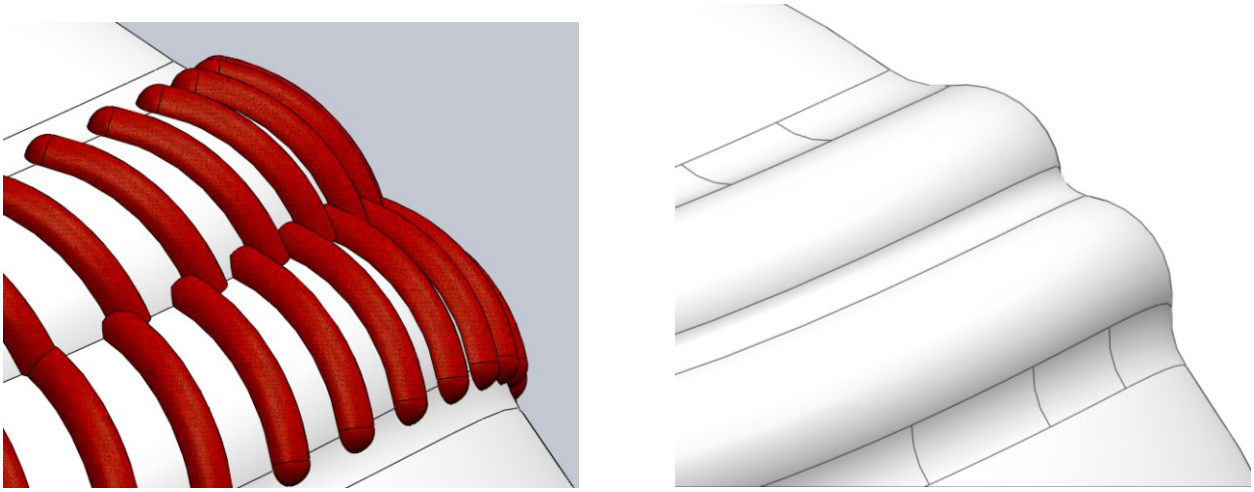

(a) (b)

Figure 2-6. (a) CAD of MLB baseball and (b) baseball geometry used in simulations

In recent investigations, the mean seam height of MLB balls was found to be approximately .031 inches (Albert et al., 2018). With a mean ball diameter of 2.85 inches, this corresponds to a seam height $h_s = D/92$. This seam height ratio is used in the present simulations, to retain as similar a ball geometry as possible to those used in real competition. The CAD model is then exported to an unstructured triangular mesh, with control points along the length of the seam, where it can be read into the ViCar3D flow solver.

Aside from the actual immersed boundary geometry, the imposition of the surface velocity due to rotation is the only difference in the computational setup between sphere and baseball simulations. Because a sphere is perfectly axisymmetric, a fixed sphere rotating about an axis through its center always occupies the same space. From a computational perspective, this means that the re-identification of solid- and fluid-cells is not necessary, and the rotation can instead be represented by a wall velocity boundary condition. The prescribed wall velocity takes the form

$$\boldsymbol{u_{sphere}} = \boldsymbol{\omega} \times \boldsymbol{r}$$

$$\boldsymbol{u_{sphere}} = \left(-\omega \cos\alpha\, r_y, \omega \cos\alpha\, r_x - \omega \sin\alpha\, r_z, \omega \sin\alpha\, r_y\right)$$

where $\boldsymbol{r} = (r_x, r_y, r_z)$ is the vector extending from the center of the sphere to a general point on the surface. With the imposition of a wall velocity, the non-trivial step of re-identifying cells for a moving boundary is avoided, making simulations of spheres more efficient. For baseball simulations, since the seam makes the body non-axisymmetric, cells must be re-identified at each time step. The surface velocity is therefore not directly imposed in this case but imposed by the movement of the boundary. Since this rotation is perfectly cyclical, identification of solid- and fluid-cells is only necessary for the first full revolution. After the first full revolution, the previous identification of cells in the computational domain is "recycled", expediting the movement of the boundary at late time steps for baseball simulations.

Simulations are performed at Reynolds numbers ($Re = \frac{U_\infty D}{\nu}$) of 500 and 1000, with dimensionless spin parameters ($\omega^* = \frac{\omega D}{2U_\infty}$) of 0.25 and 0.5. The spin axis α is varied from 0° to 90°, or streamwise and transverse rotation, respectively. Two different seam heights are used: a "small" seam which is the height of a typical MLB ball ($h_s = D/92$), and a "large" seam which is twice as large ($h_s = D/46$). Simulations are run for 100 convective time units ($\tau = tU_\infty/D$), approximately 8 sphere revolutions for $\omega^* = 0.25$, or 16 revolutions for $\omega^* = 0.5$.

2.4 SIMULATION SETUP – FLETTNER ROTORS

2.4.1 SURFACE SUCTION

In the simulations of flows past rotating cylinders, two primary areas are investigated. First, simulations are performed investigating the effect of surface suction on 3D Flettner rotors in a uniform flow. Figure 2-7 shows a schematic of the problem setup. Similar to baseball

aerodynamics simulations, the spin ratio is defined as $\omega^* = \frac{\omega D}{2U_\infty}$. A radial surface velocity is applied on the cylinder in a suction zone which is 45° wide, located 120° clockwise from the front of the cylinder. The suction ratio $\gamma = \frac{U_{suction}}{U_\infty}$ describes the strength of the suction in relation to the free-stream velocity.

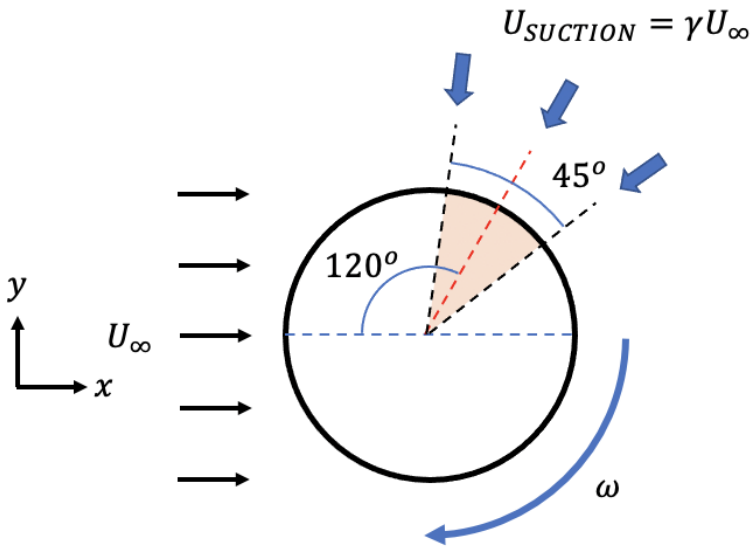

Figure 2-7. 2D schematic of the problem setup for a Flettner rotor with suction

A computational domain with size $22D \times 18D \times 10D$, with D the diameter of the cylinder. Figure 2-8 shows a 3D isometric view of the computational domain used.

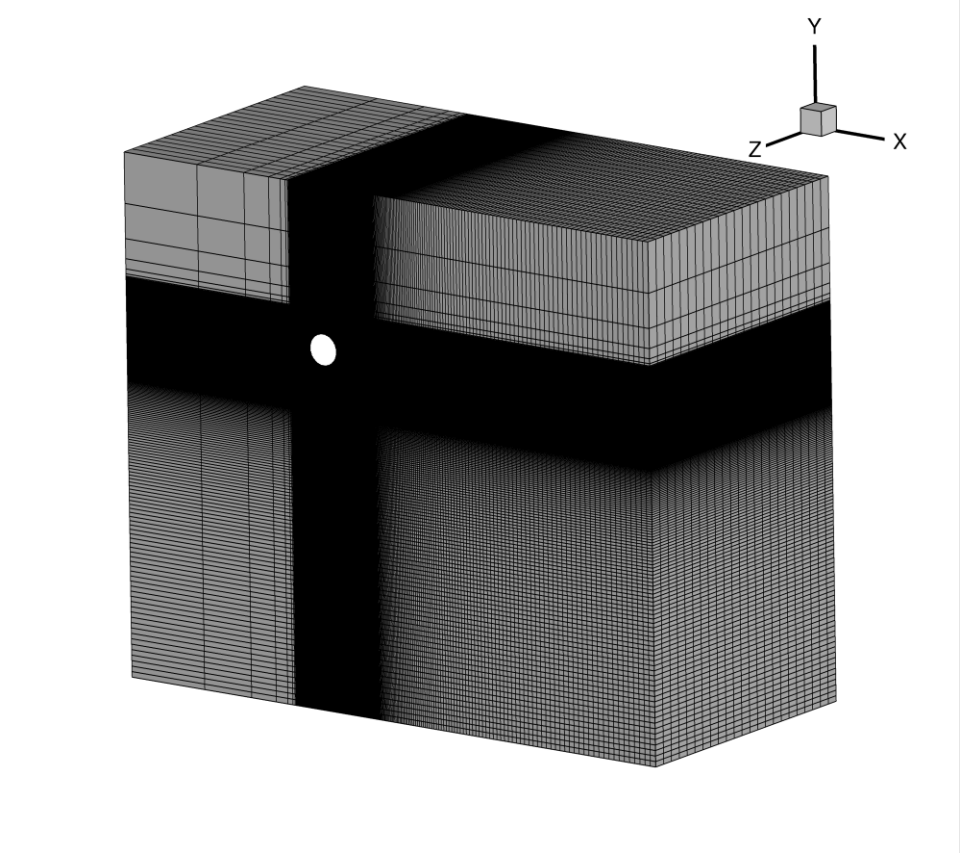

Figure 2-8. Computational domain used in Flettner rotor with suction simulations

The domain is comprised of approximately 1.5 million cells, with 256 points in the x- and y-directions, and 24 points in the z-direction. Figure 2-9 shows a cross-section of the computational domain in the xy-plane. A fine-mesh region of size $3D \times 3D$ in the xy-plane is used near the cylinder, with uniform grid spacing $\Delta x = D/48$. The grid is stretch rapidly upstream of the cylinder, and slowly stretched with a hyperbolic tangent function downstream of the cylinder to maintain a stretching ratio $\frac{\Delta x_{i+1}}{\Delta x_i} \approx 3.0\%$. Similar to the mesh used for sphere simulations, the cylinder is placed in the "upper-left" portion of the fine-mesh region, $0.75D$ from the edge of this region in the x- and y-directions. In the z-direction, along the length of the cylinder, a uniform

grid spacing is used. The length of the cylinder extends through the entirety of the z-direction, with an aspect ratio $\frac{L}{D} = 10$.

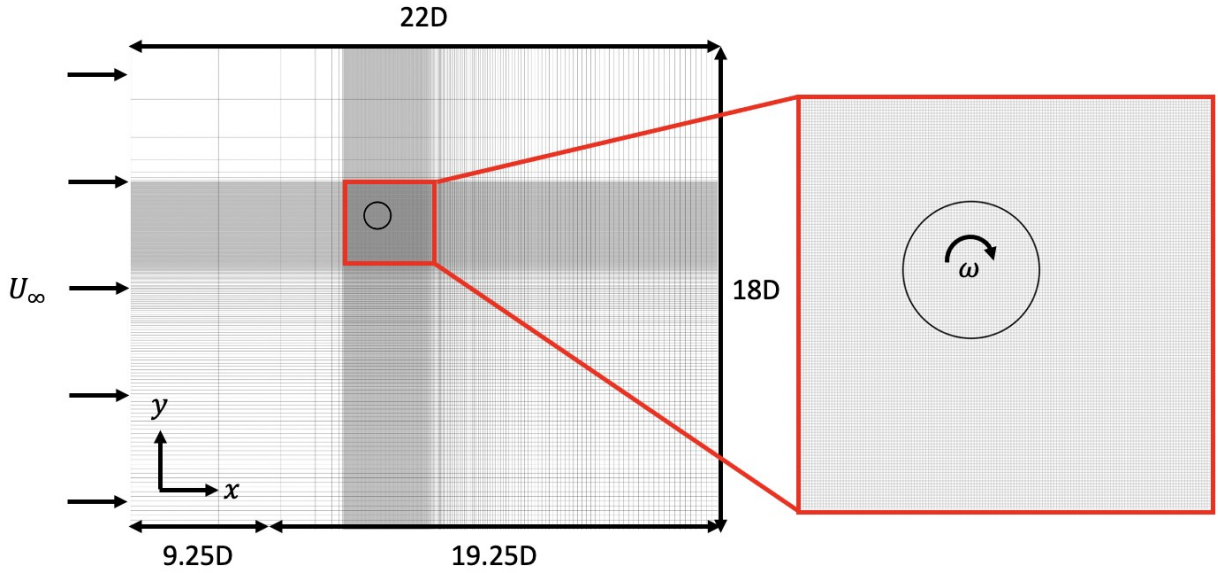

Figure 2-9. 2D view (xy-plane) of overall computational domain (left) with inset (right) of fine-mesh region near the cylinder

A uniform Dirichlet boundary condition is imposed on the inlet ($x = 0$), such that $\boldsymbol{u} = (U_\infty, 0,0)$. A zero-gradient Neumann boundary condition is imposed on the outlet ($x = 22D$) and both walls in the y-direction ("bottom" and "top"). A symmetry boundary condition is applied on both walls in the z-direction ("front" and "back"), or both ends of the cylinder. On the surface of the cylinder, a wall boundary condition is imposed for the rotation, such that

$$\boldsymbol{u_{cylinder}} = \boldsymbol{\omega} \times \boldsymbol{r}$$

$$\boldsymbol{u_{cylinder}} = \left(-\omega \cdot r_y, \omega \cdot r_x, 0\right)$$

where $\boldsymbol{r} = (r_x, r_y)$ is the vector extending from the center of the cylinder to a general point on the surface. A no-slip boundary condition is imposed everywhere on the surface except in the suction region, where

$$\boldsymbol{u_{cylinder}} = (-\frac{\gamma U_\infty r_x}{R}, -\frac{\gamma U_\infty r_y}{R}, 0)$$

where γ is the suction ratio and R is the cylinder radius.

Simulations are performed at a Reynolds number of 200, with spin ratios from 2.5 to 3.5. The suction ratio γ is varied from 0 to 0.5. Simulations are run for 62.5 convective time units ($\tau = tU_\infty/D$), at which point the flow reaches steady state for all parameters considered.

2.4.2 TAPERED CYLINDERS

The second type of Flettner rotor investigated in this study is the spanwise profile of the cylinder, or the "taper" of the cylinder. Figure 2-10a shows a schematic of the problem setup, with a "straight" cylinder (no variation in diameter along the length) and a "tapered" cylinder (diameter varies linearly along the length). The grid is identical to the one used in the surface suction simulations in the x- and y-directions but has 48 grid points instead of 24 in the z-direction, due to the increased three-dimensionality of flows with tapered cylinders. Additionally, a gap between the ends of the cylinder and the front and back walls is included, equal to 10% of the cylinder length, so the domain size is $12D$ in the z-direction.

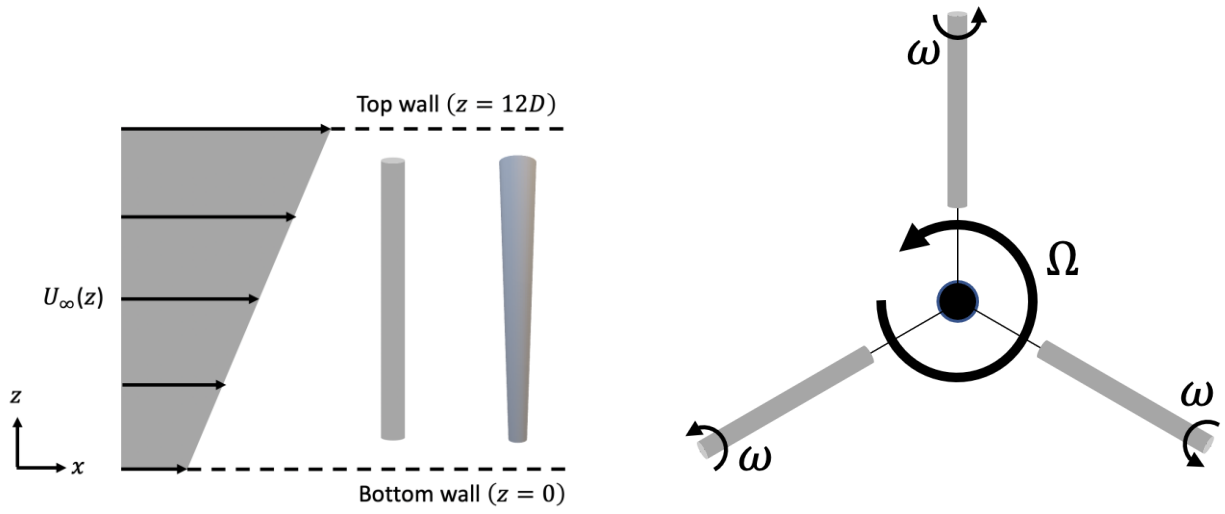

Figure 2-10. (a) Shear inflow BC and cylinder profiles in xz-plane, and gap between boundaries and cylinder ends (b) "Flettner drone" with cylinder rotating about a central point

In this problem, instead of the uniform inflow velocity in the suction investigation, a shear inflow boundary condition is used, with velocity varying along the length of the cylinder. This is to simulate the effect of rotation, as shown in Figure 2-10b. Because the main quantities of interest are force coefficients, which are normalized be the quantity $\frac{1}{2}\rho A U^2$, a shear inflow profile is used such that the integral quantity $\int_0^1 U\left(z^* = \frac{z}{L}\right)^2 dz^*$ is equal between a uniform inflow and a shear inflow. With the uniform inflow boundary condition given by $U(z^*) = 1$, the equivalent shear inflow condition is $U(z^*) = z^* + 0.4574$, such that the velocity at the "bottom" of the cylinder is 0.4574 and the velocity at the "top" of the cylinder is 1.4574. Diameter ratios $\left(\frac{D_{top}}{D_{bottom}}\right)$ of 2:1 and 3:1 are simulated, with the larger diameter at the "fast" end of the cylinder. Boundary conditions are similar to the surface suction simulations with the exception of the inflow, and a similar boundary conditions on the cylinder with the exception of the suction velocity.

CHAPTER 3. RESULTS AND DISCUSSION – BASEBALL AERODYNAMICS

3.1 ROTATING SPHERES

Simulations are for rotating spheres and spheres with seams are performed for three Reynolds number and spin parameter combinations: $Re = 500$, $\omega^* = 0.25$; $Re = 500$, $\omega^* = 0.5$; and $Re = 1000$, $\omega^* = 0.25$. Poon et al. (2014) and others have characterized and mapped the flows past spheres for $Re = 100 - 1000$, $\omega^* \leq 1.2$. Figure 3-1 shows the present studies in the context of the flow regimes identified by previous literature.

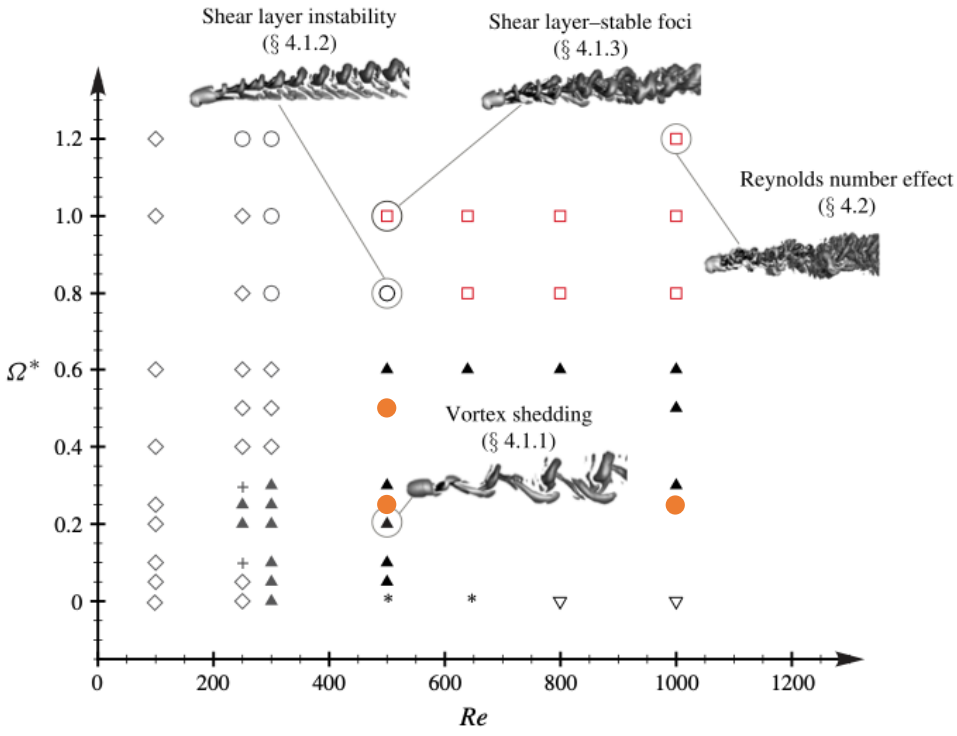

Figure 3-1. Different flow regimes for transversely rotating spheres, from Poon et al. (2014). Orange circles (●) indicate parameters sampled in the present study.

3.1.1 FLOW STRUCTURES

The flow past a rotating sphere at $Re = 500$, $\omega^* = 0.25$ is investigated for $\alpha = 0°, 15°, 30°, 45°, 60°, 75°$, and $90°$. For transverse rotation ($\alpha = 90°$), a "vortex shedding" regime has been reported at $\omega^* = 0.2$ (Poon et al., 2014), characterized by horseshoe shaped vortices shed downward from the sphere, with opposing induced vortices, both of which are symmetric about the yz-plane. While the effect of rotation axis has been studied at $Re = 300$ (Poon et al., 2010), the effect of rotation axis is less well studied at higher Re. Figure 3-2 shows the flow structures across the range of α sampled. Flow structures are identified by the maximum imaginary component of the eigenvectors (λ_{max}) of the velocity gradient tensor $\nabla \boldsymbol{u}$ (Chong et al., 1990), with isosurfaces of $\lambda_{max} = 0.25$ plotted. Isosurfaces are colored by velocity magnitude $\overline{\boldsymbol{u}}$. Qualitatively, the flow structures at $\alpha = 90°$ are well matched to those observed by Poon et al., with periodic horseshoe vortex shedding and is symmetric about the yz-plane. The flow structures are largely the same at $\alpha = 75°$, but are no longer planar symmetric due to the slight asymmetry of the sphere's rotation. At $\alpha = 45°$, the wake retains some of the features from higher α, but is noticeably deflected in the $+x$-direction. At lower α of 0° and 15°, the wake loses the periodic horseshoe vortex shedding structure, and is instead characterized by elongated threads which spiral about the streamwise axis, resulting in near zero time-averaged lift in the x- and y-directions. This behavior is similar to that observed at lower Re. Looking at the time-average streamwise velocity contours, there is a clear trend of increased asymmetry in the xz-plane as α tends to 45°. At $\alpha = 0°$ and 90°, the mean flow is planar symmetric, with $\alpha = 0°$ being axisymmetric.

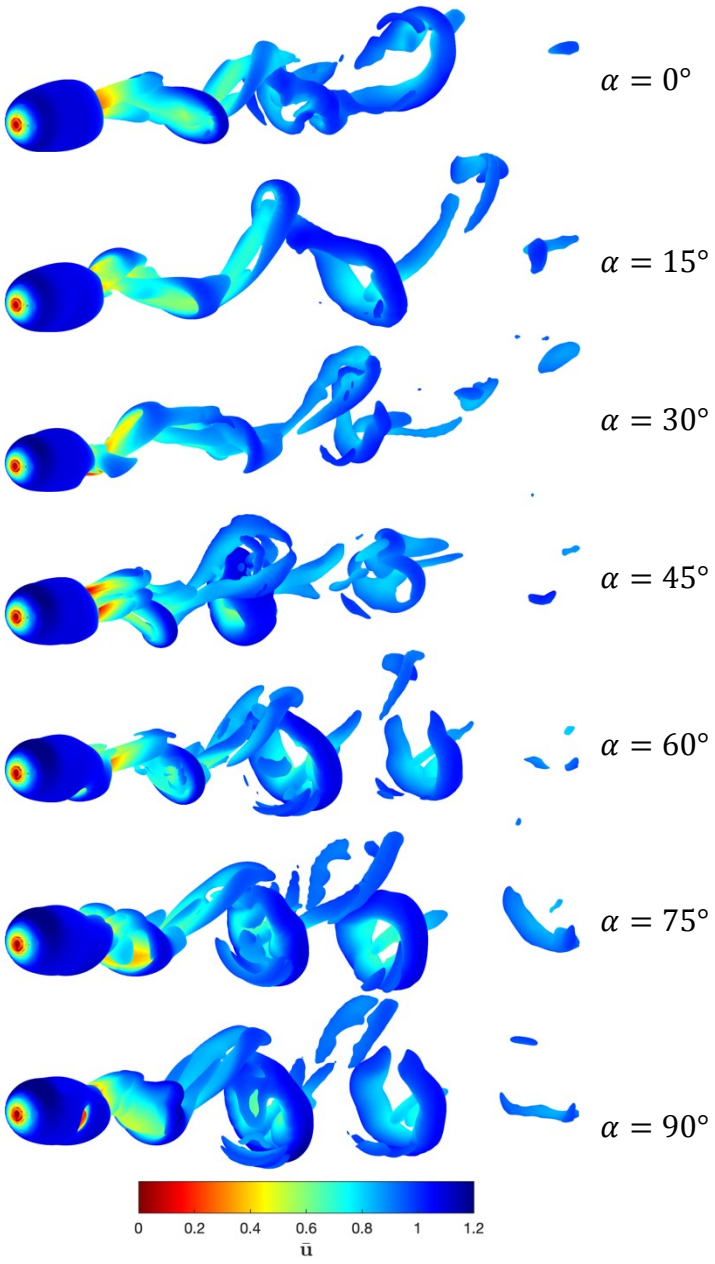

Figure 3-2. Isosurface plots at $Re = 500, \omega^* = 0.25$, colored by $\bar{\boldsymbol{u}}$

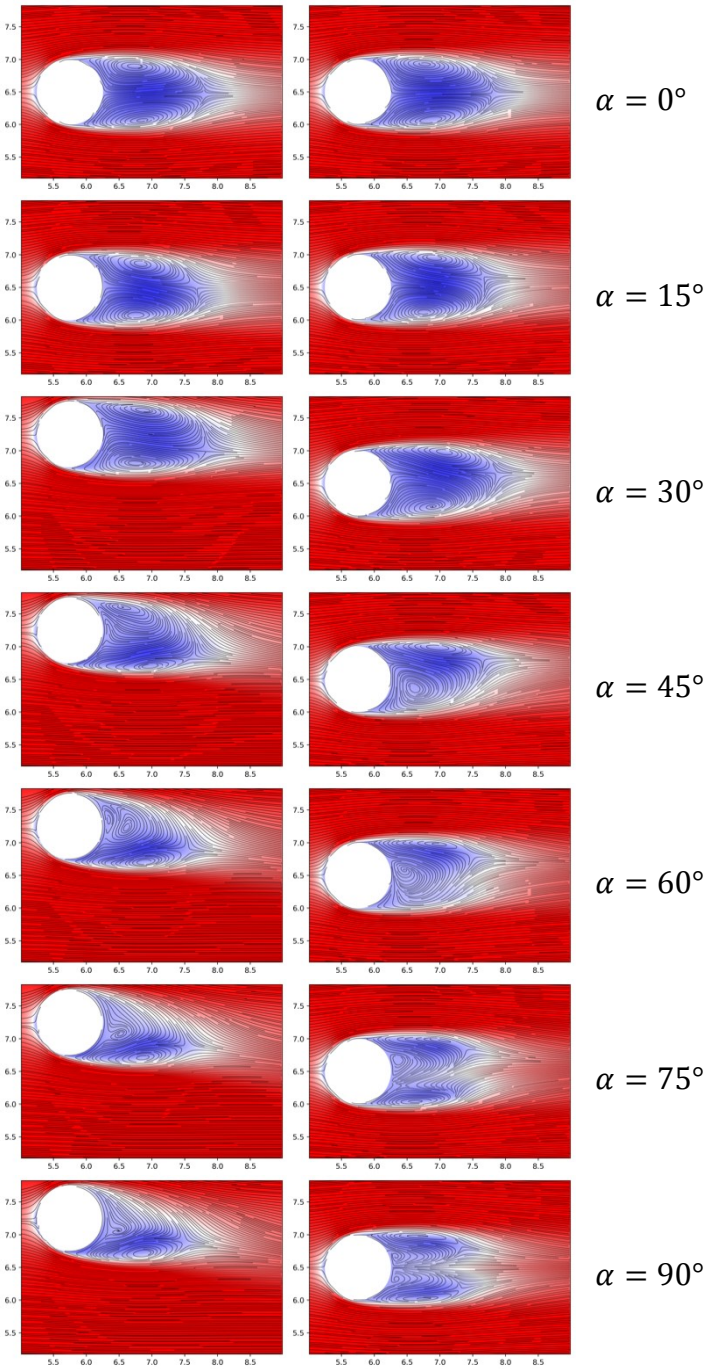

Figure 3-3. Time-averaged streamlines with streamwise velocity contours in yz-plane (left) and xz-plane (right) for $Re = 500$, $\omega^* = 0.25$

The flow past a rotating sphere at $Re = 500$ and an increased $\omega^* = 0.5$ are investigated for $\alpha = 45°$ and 90°. The flow remains in the "vortex shedding" regime as observed by Poon et al. for ω^* up to 0.6. Figure 3-4 shows the flow structures at the two α sampled.

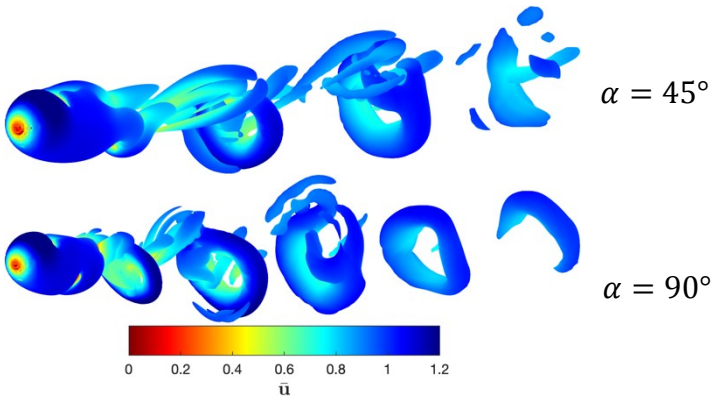

Figure 3-4. Isosurface plots at $Re = 500, \omega^* = 0.5$, colored by $\bar{\boldsymbol{u}}$

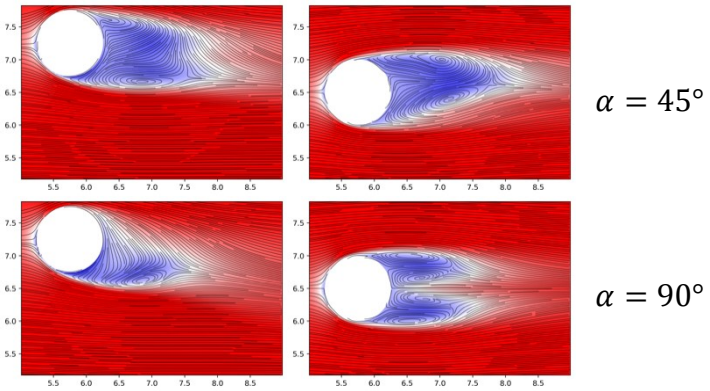

Figure 3-5. Time-averaged streamlines with streamwise velocity contours in yz-plane (left) and xz-plane (right) for $Re = 500$, $\omega^* = 0.5$

For transverse rotation, the horseshoe vortex shedding remains but is no longer as planar symmetric as at lower ω^*. The wake is again noticeably deflected in the $+x$-direction at $\alpha = 45°$. In both cases, the mean recirculation region is shortened in comparison to $\omega^* = 0.25$.

At $Re = 1000$ and $\omega^* = 0.25$, the flow regime becomes quite different. At earlier times, the flow is similar to the periodic, symmetric vortex shedding seen at $Re = 500$ for transverse rotation. However, at later times in the simulation the flow in the near wake region is much less periodic, and the wake becomes more chaotic as it is convected downstream. At $\alpha = 45°$, the wake is again deflected in the $+x$-direction but does not retain as much of the flow structure from the $\alpha = 90°$ case as at lower ω^*. Figure 3-6 shows snapshots the flow structures at the end of the simulation.

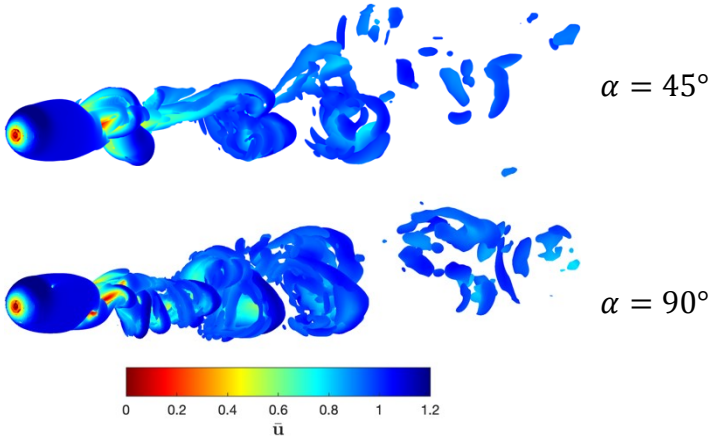

Figure 3-6. Isosurface plots at $Re = 1000, \omega^* = 0.25$ for $\alpha = 45°, 90°$, colored by $\bar{\boldsymbol{u}}$

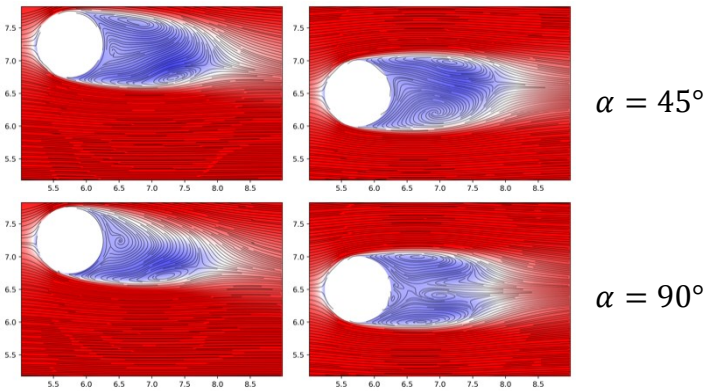

Figure 3-7. Time-averaged streamlines with streamwise velocity contours in yz-plane (left) and xz-plane (right) for $Re = 1000$, $\omega^* = 0.25$

3.1.2 FORCE COEFFICIENTS

Force coefficients are reported at different across the range of simulations of rotating spheres. Figure 3-8 shows the time-varying drag, lift, and side-force coefficients at $Re = 500$, $\omega^* = 0.25$, for $\alpha = 0° - 90°$, while Figure 3-9 shows the mean quantities, averaged over the final half of the simulation (50 time units). The lift C_{L_y} shows a clear increase with an increase in α – as expected from a Magnus effect model, which predicts that the lift scales linearly with the transverse component of rotation. C_D shows an increase with α for $\alpha \geq 45°$, but decreases from $\alpha = 0°$ to 30° - a departure from the trend observed by Poon et al. (2010). This phenomenon is discussed further in Section 3.2. The side-force C_{L_x} has fluctuations which are non-trivial in comparison to C_{L_y} for all α except 90°, where the side-force is approximately 0 throughout the simulation. At both $\alpha = 0°$ and 90°, the time-averaged side-force is approximately zero, and the side-force peaks in magnitude at $\alpha = 45°$, with $\left|\frac{C_{L_x}}{C_{L_y}}\right| = 37.9\%$.

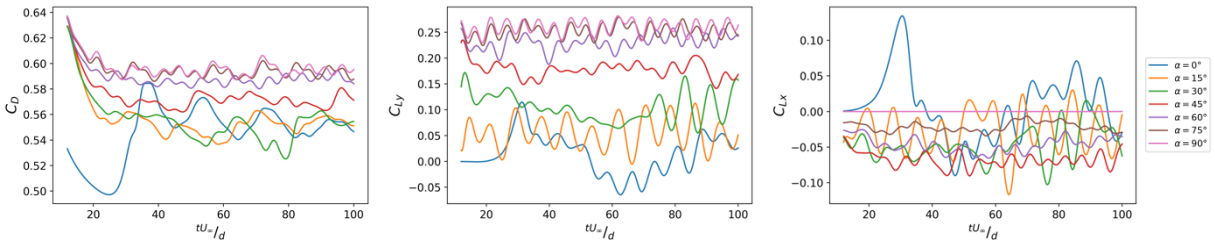

Figure 3-8. Time history of drag (left), lift (middle), and side-force (right) coefficients for sphere at $Re = 500$, $\omega^* = 0.25$

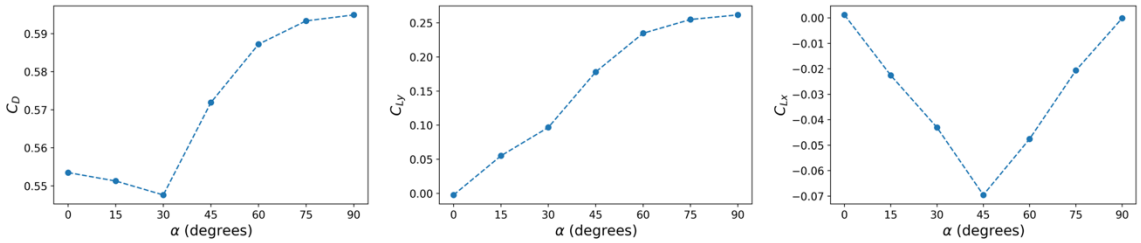

Figure 3-9. Time-averaged drag (left), lift (middle), and side force (right) coefficients for sphere at $Re = 500$, $\omega^* = 0.25$

Force coefficients for an increased ω^* ($Re = 500$, $\omega^* = 0.5$) and an increased Re ($Re = 1000, \omega^* = 0.25$) are reported for $\alpha = 45°$ and 90°. With increased rotation of the sphere, both the drag and lift increase in magnitude. The side-force, which was zero throughout the time of the simulation at $\omega^* = 0.25$, is initially zero but begins to have non-zero fluctuations in time during the last half of the simulation. This correlates with the slight asymmetry observed in the wake structures due to increased instability from higher rotation rates. For the $\alpha = 45°$ case, the side force is again non-trivial, with $\left|\frac{C_{Lx}}{C_{Ly}}\right| = 43.0\%$. At $Re = 1000$, drag and lift are reduced from the $Re = 500$ case, with the side force becoming more unsteady at $\alpha = 90°$. At $\alpha = 45°$, the side-force is again significant, though smaller than at $Re = 500$, with $\left|\frac{C_{Lx}}{C_{Ly}}\right| = 23.2\%$.

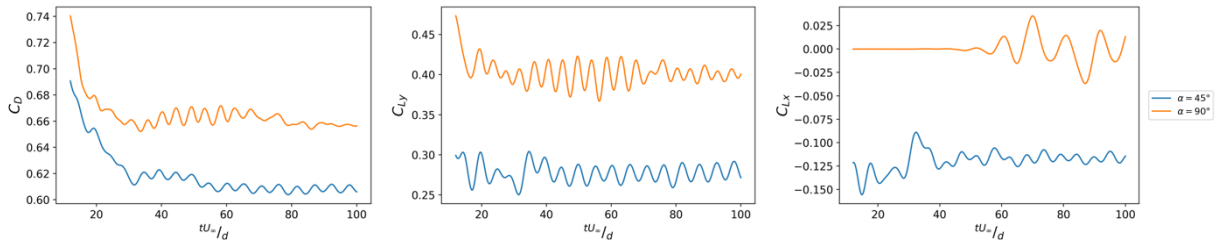

Figure 3-10. Time history of drag (left), lift (middle), and side-force (right) coefficients for sphere at $Re = 500$, $\omega^* = 0.5$

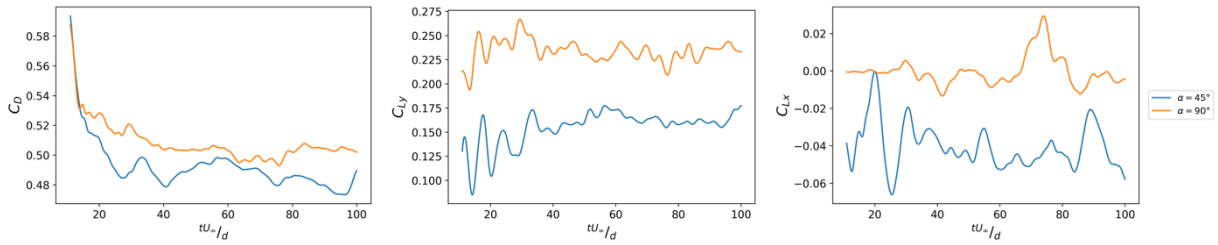

Figure 3-11. Time history of drag (left), lift (middle), and side-force (right) coefficients for sphere at $Re = 1000$, $\omega^* = 0.25$

3.2 BASEBALL AERODYNAMICS

In this section, we report simulations of baseballs for the same flow conditions as the spheres in Section 3.1. For $Re = 500$, $\omega^* = 0.25$, two different seam orientations are simulated – "four-seam" and "two-seam", traditionally the most used seam configurations used by baseball pitchers. Figure 3-11 shows a graphical representation of the two different seam orientations for $\alpha = 90°$. At $Re = 500$, $\omega^* = 0.5$ and $Re = 1000$, $\omega^* = 0.25$, a four-seam orientation is simulated. At $Re = 1000$, $\omega^* = 0.25$, simulations are performed for a "small" seam ($h_s = 0.31"$) and a "large" seam ($h_s = 0.62"$). The effect of the seam is discussed in terms of the effect on qualitative flow features as well as aerodynamics force coefficients, which affect the trajectory of pitched balls in flight.

(a)

(b)

Figure 3-12. Rotation of a baseball in (a) two-seam orientation and (b) four-seam orientation

3.2.1 FLOW STRUCTURES

For $Re = 500$, ω^*, simulations are performed on baseballs with a four-seam and two-seam orientation. Figure 3-13 shows a comparison of the flow structures at $\alpha = 90°$ between a sphere and baseballs. While flow structures in the wake of both four- and two-seam baseballs remain in the "vortex shedding" regime seen for a transversely rotating sphere, the seam introduces asymmetry about the yz-plane not observed for a sphere with no seam, especially in the four-seam case. In the two-seam case the flow is much more symmetric, as the seam remains symmetric about the yz-plane for a transversely rotating two-seam ball while it is asymmetric for a four-seam ball.

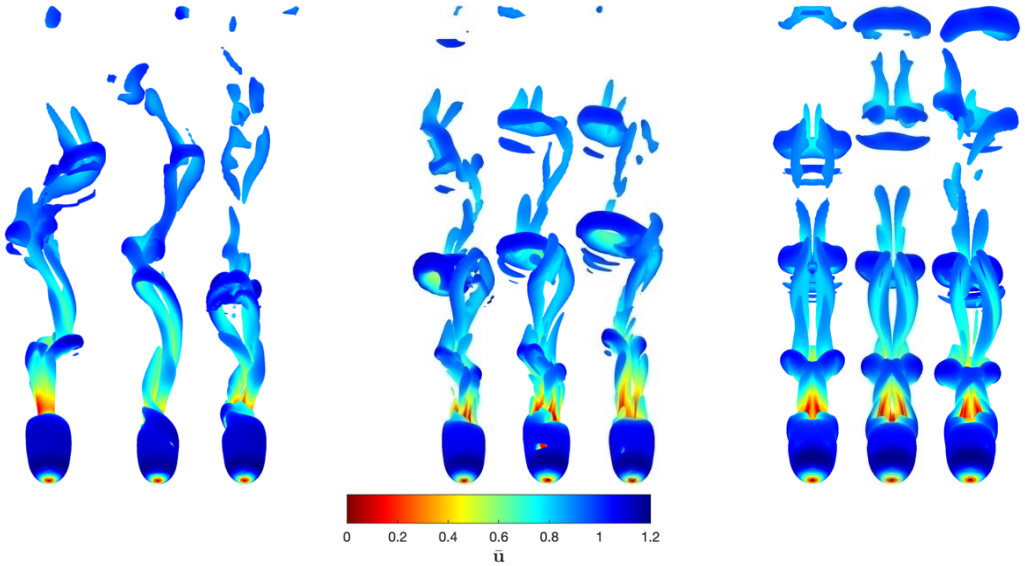

(a) (b) (c)

Figure 3-13. Isosurface plots at $Re = 500, \omega^* = 0.25$ at (a) $\alpha = 0°$, (b) $\alpha = 45°$, (c) $\alpha = 90°$, colored by $\bar{u}$. Spheres are shown at left, two-seams at middle, and four-seams at right.

Figure 3-14 shows streamlines and mean streamwise velocity comparisons between spheres and the two seam orientations considered. Though instantaneous flow structures are somewhat varied, mean flow quantities show very little difference between a sphere and either baseball seam

orientation. This trend is also present in the time-averaged force coefficients with some exceptions, which will be discussed below.

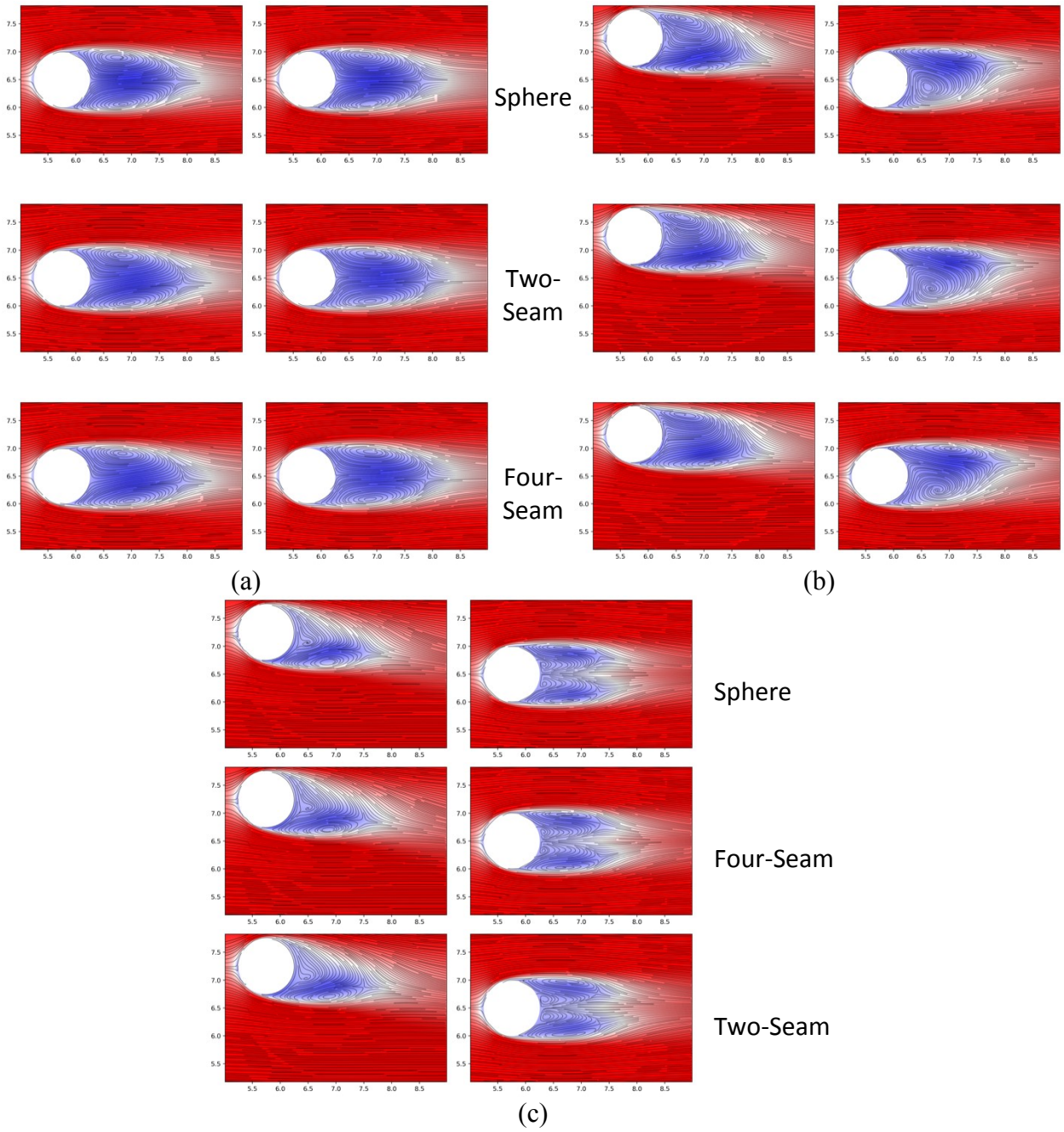

Figure 3-14. Time-averaged streamlines with streamwise velocity contours in yz-plane (left) and xz-plane (right) for at (a) $\alpha = 0°$, (b) $\alpha = 45°$, (c) $\alpha = 90°$ for $Re = 500$, $\omega^* = 0.25$

At $Re = 500$, $\omega^* = 0.5$, the vortex shedding regime observed for spheres with transverse rotation is again seen for a four-seam baseball. The wake retains the slight asymmetry not seen at lower ω^*, though the side-force coefficients average to zero in time. At $\alpha = 45°$, the wake is again deflected to the $+x$-direction and the flow structures are largely the same, though the deflected horseshoe vortices are not as prominent for the four-seam baseball case in comparison to a sphere.

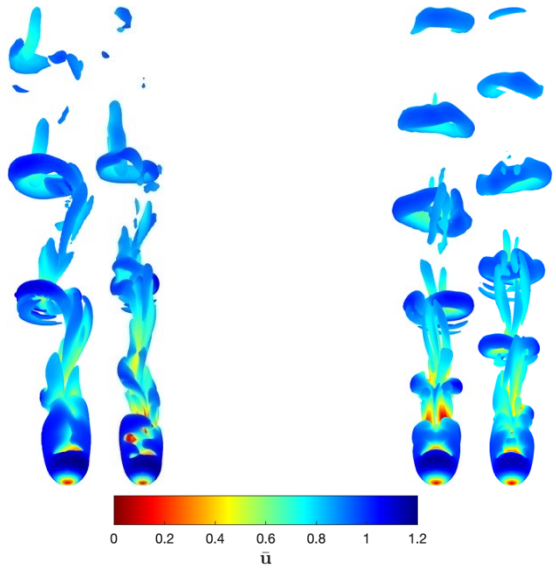

(a) (b)

Figure 3-15. Isosurface plots at $Re = 500, \omega^* = 0.5$ at (a) $\alpha = 45°$ and (b) $\alpha = 90°$, colored by $\bar{\boldsymbol{u}}$. Spheres are shown at left and four-seams at right.

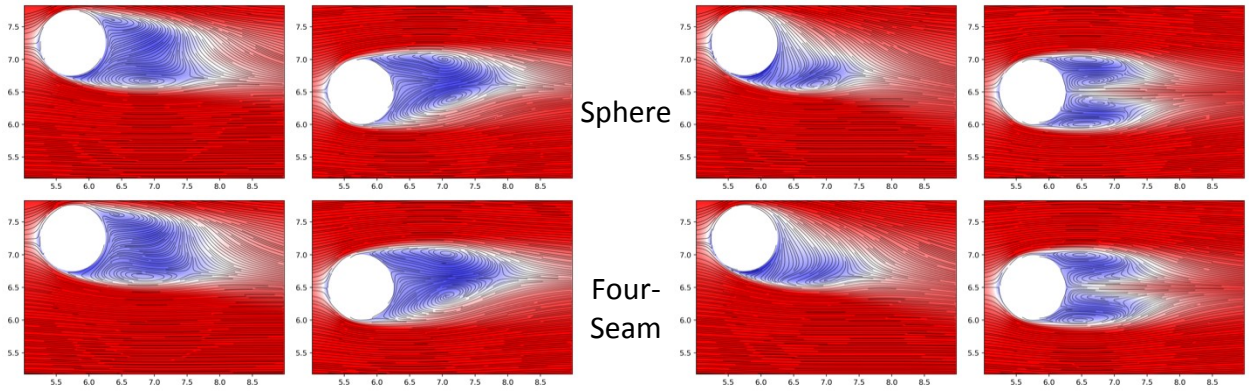

Figure 3-16. Time-averaged streamlines with streamwise velocity contours in yz-plane (left) and xz-plane (right) for at (a) $\alpha = 45°$, (b) $\alpha = 90°$ for $Re = 500$, $\omega^* = 0.5$

At $Re = 1000$, $\omega^* = 0.25$, simulations are performed for a four-seam baseball with a "small" seam (approximately the height of an MLB seam) as in the simulations above, as well as a "large" seam, which is twice the height of the small seam. At this higher Reynolds number, the effects of the seam are more apparent. The flow past a sphere is already more chaotic and turbulent than at lower Reynolds number, but the seam appears to make the wake even more chaotic, as evidenced by the flow structures for both $\alpha = 45°$ and $\alpha = 90°$. The recirculation region noticeably shortens with an increase in seam height, and the mean flow for a large seam at $\alpha = 45°$ is noticeably more deflected in the $+x$-direction than the sphere or small seam cases.

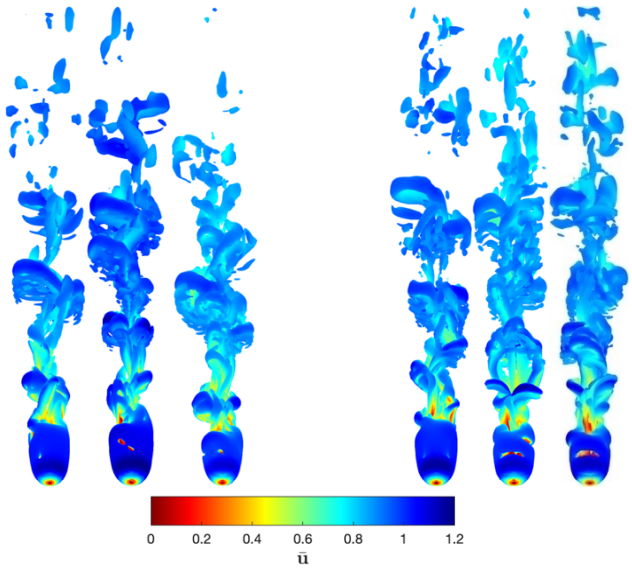

(a) (b)

Figure 3-17. Isosurface plots at $Re = 1000, \omega^* = 0.25$ at (a) $\alpha = 45°$ and (b) $\alpha = 90°$, colored by $\bar{\boldsymbol{u}}$**.** Spheres are shown at left, small seams at middle, large seams at right.

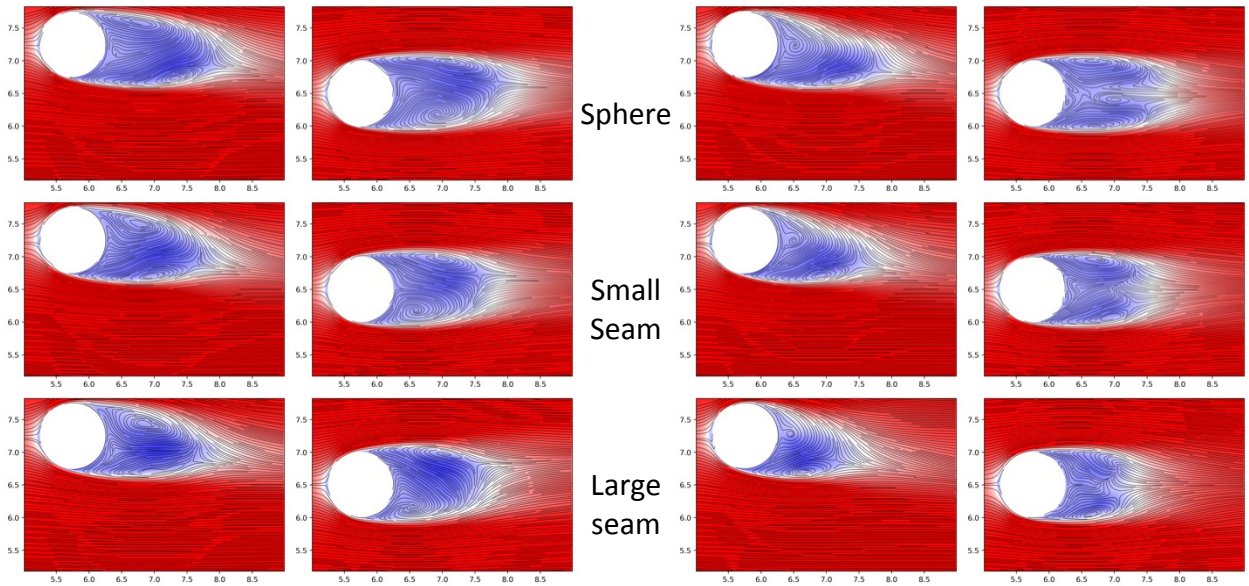

(a) (b)

Figure 3-18. Time-averaged streamlines with streamwise velocity contours in yz-plane (left) and xz-plane (right) for at (a) $\alpha = 45°$, (b) $\alpha = 90°$ for $Re = 1000$, $\omega^* = 0.25$

3.2.2 FORCE COEFFICIENTS

Force coefficients for baseball simulations are reported and compared to the forces on rotating spheres. Figure 3-19 shows the drag, lift, and side-force coefficients at $Re = 500$, $\omega^* = 0.25$ at $\alpha = 90°$. Both drag and lift track very closely between a sphere, two-seam baseball, and four seam baseball, and the time-averaged values are nearly identical. The side-force reflects trends noted in the flow structures in the previous section. While the side-force on a sphere is zero throughout the simulation, the side-force on a four-seam baseball has small but non-trivial fluctuations. However, a change in the seam orientation to two-seam results in a significantly dampened side-force signal in time, largely attributable to the unique planar symmetry of the ball with this orientation rotating about the transverse axis. Time-averaged force quantities are reported for $\alpha = 0° - 90°$. The non-monotonic behavior of the drag with α is not seen with two-seam or four-seam baseball as it is with spheres. Interestingly, there are other phenomena in which the flow past a sphere exhibits unexpected behavior, while a baseball behaves more conventionally. Briggs (1959) and others have observed that a rotating sphere may exhibit an "anti-Magnus" effect, where the lift direction is opposite what is predicted by the Magnus effect, while no such effect has been reported for baseballs (Nathan, 2008). This is perhaps another instance of the seam "stabilizing" the behavior of flows past rotating spheres. Predictably, the drag is slightly higher for a baseball than for a sphere due to the seam. Lift values are very close between all three cases, increasing from zero at $\alpha = 0°$ to a maximum at $\alpha = 90°$. The average side-force values vary slightly between the three cases, though a maximum magnitude in side-force occurs at $\alpha = 45°$ for spheres and both seam orientations. Interestingly, the seam does not appear to enhance the side-force at this regime, even reducing the side-force at $\alpha = 45°$ in the case of a four-seam orientation.

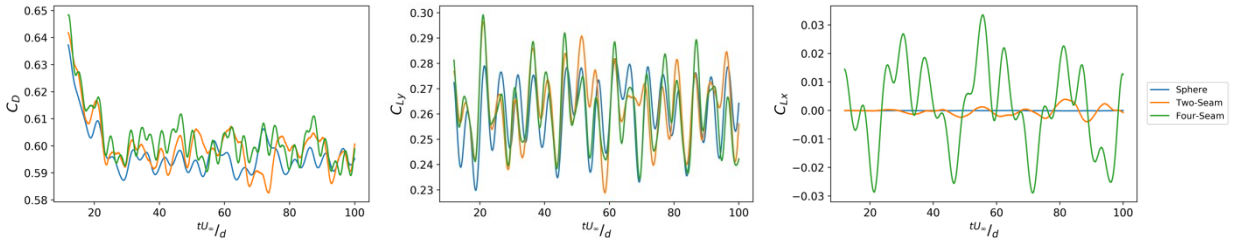

Figure 3-19. Time history of drag (left), lift (middle), and side-force (right) coefficients for sphere and baseballs at $Re = 500$, $\omega^* = 0.25$, $\alpha = 90°$

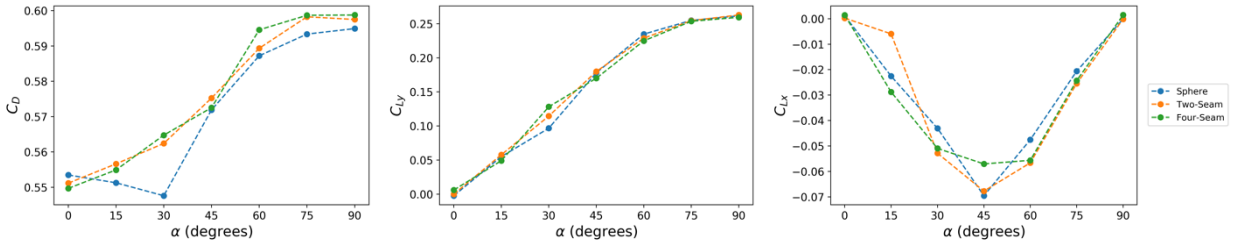

Figure 3-20. Time-averaged drag (left), lift (middle), and side force (right) coefficients for sphere and baseballs at $Re = 500$, $\omega^* = 0.25$

Figure 3-21 shows time-average force comparisons between a sphere and a four-seam baseball at the three Re and ω^* regimes investigated. At $Re = 500$, $\omega^* = 0.5$, the trend is similar to at $\omega^* = 0.25$. For a four-seam orientation, the seam has little effect on drag and lift, with time-averaged values nearly identical to a sphere. While at $\omega^* = 0.25$, a four-seam orientation reduces the side-force at $\alpha = 45°$ by 18%, at $\omega^* = 0.5$ the side-forces are within 1% of each other. The largest effect of a seam at this size is when the Reynolds number is increased to 1000. Here, the seam increases the drag by roughly 6%, approximately 10 times the increase in drag caused by the seam at $Re = 500$.

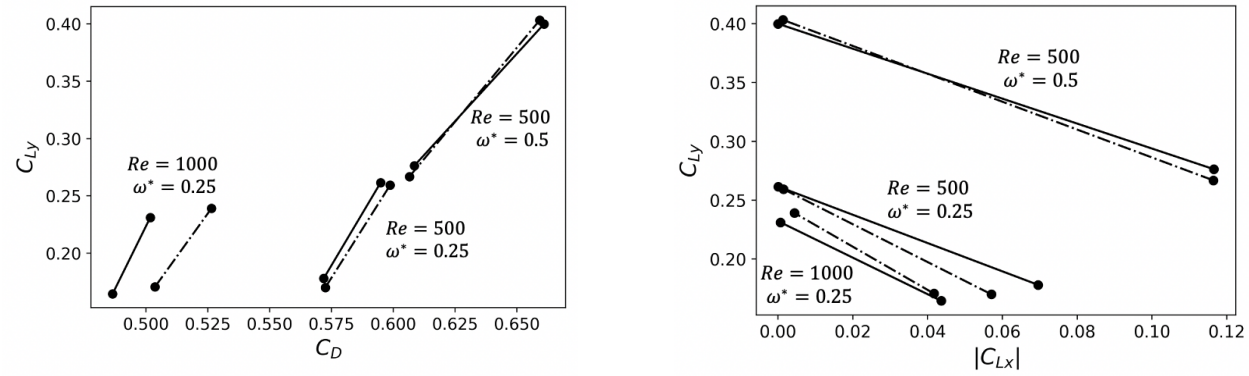

Figure 3-21. Drag, lift, and side-force trends between spheres (solid lines) and four-seam baseballs (dashed lines) at $a = 45°, 90°$

Looking at the effect of different seam heights at $Re = 1000$, there is a clear effect of increasing the seam height on all force coefficients. A larger seam yields a slight increase in lift, with a more significant increase in drag. The side force, which is similar in magnitude between a sphere and a baseball with a small seam, increases by 40% for a large seam at $\alpha = 45°$. The trend of increased side force with increased Reynolds number and seam height indicates that as the boundary layer thickness decreases and the seam height becomes larger relative to the boundary layer size, the seam has a greater influence on the boundary layer and, at intermediate α such as 45°, can enhance asymmetries in separation on either side of the ball, leading to a greater lateral side-force.

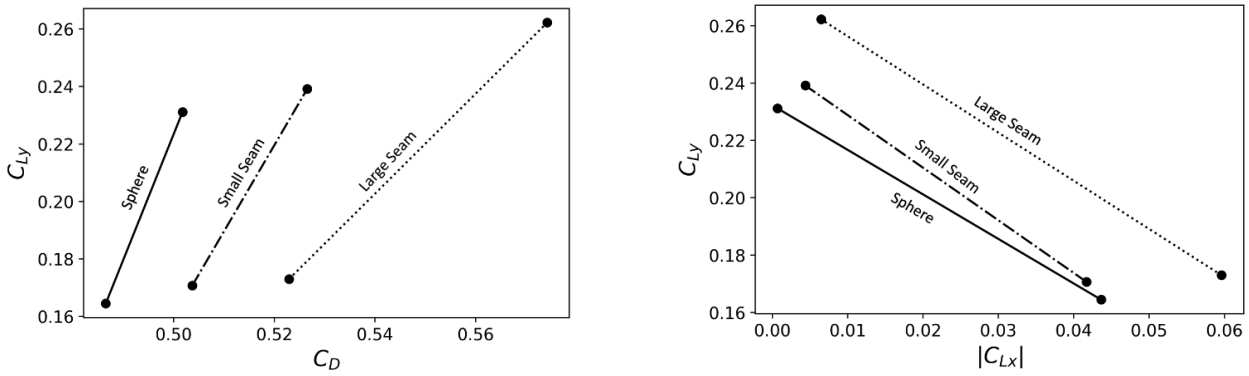

Figure 3-22. Drag, lift, and side-force trends between a sphere, small seam baseball, and large seam baseball at $Re = 1000$, $\omega^* = 0.25$ for $\alpha = 45°, 90°$

In while an increased seam height does cause an increased side-force, it is clear that the side-force is present even without any seam at all. It is likely that at the higher Reynolds numbers at which the game of baseball is played, the seam is more important in the "side-force" or "wake-shifting" phenomenon due to further decrease in the boundary layer size. However, it is apparent that at more moderate Reynolds numbers of $500 - 1000$, this phenomenon is more attributable to the spin axis α than the seam itself. At $\alpha = 45°$ and adjacent values, the side-force is sufficient to significantly alter the flight of balls in motion, with or without the presence of a seam. In the following section, the implications of the aerodynamic forces obtained from the present simulations on the trajectory and movement of pitched baseballs is discussed.

3.2.3 PITCHED BASEBALL TRAJECTORY EXAMPLE

In this section, the present findings are used in a sample calculation of the trajectory and total movement of pitches thrown with different spin axes and seam orientations. Figure 3-23 shows the pitch movement profile of two-seam and four-seam baseballs thrown with different spin axes, using data obtained from simulations at $Re = 500$, $\omega^* = 0.25$. Calculations are done for a

typical MLB fastball velocity of 90 mph released 55 feet from home plate from a right-handed pitcher with an "over-the-top" (or 12:00) arm slot. Pitch movements are reported with the movement due to gravity subtracted (e.g., a pitch with zero lift would have 0" of horizontal and vertical movement). For $\alpha = 45°$, the side force contributes roughly 6 inches (more than 2 ball diameters) of horizontal movement not accounted for by the Magnus force. Figure 3-24 shows an example of final pitched ball locations for selected α relative to the "strike zone". For $\alpha = 45°$, a Magnus-only model would predict the ball to land in the middle of the strike zone, but the side-force causes the ball nearly outside the strike zone. In a so-called "game of inches", this could represent a significant competitive advantage for a pitcher who is able to make use of the side=force.

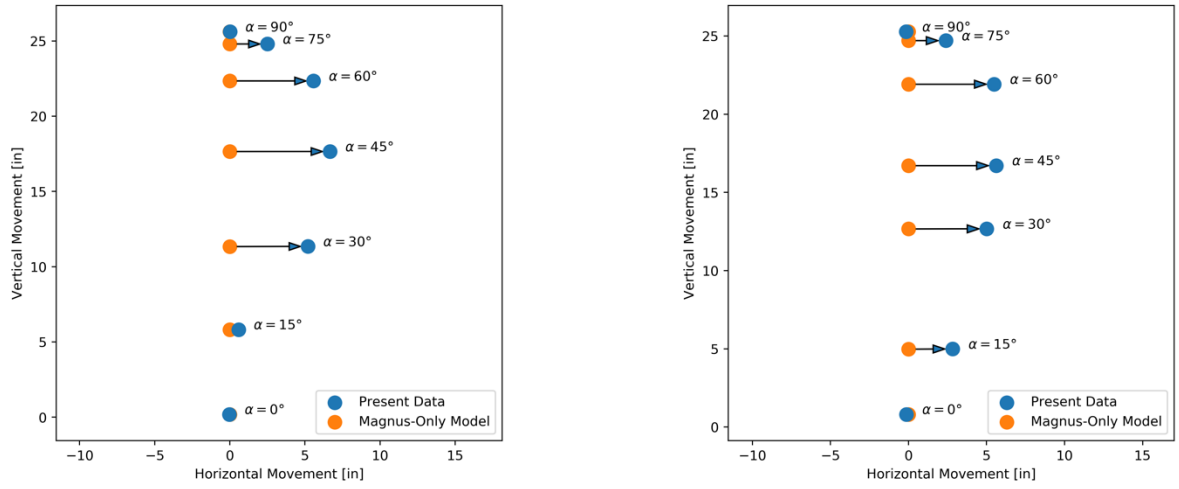

(a) (b)

Figure 3-23. Total pitch movement for (a) two-seam and (b) four-seam pitched baseball, in comparison to a "Magnus-only" model with no side-force. Arrows represent the "additional" movement from the side-force.

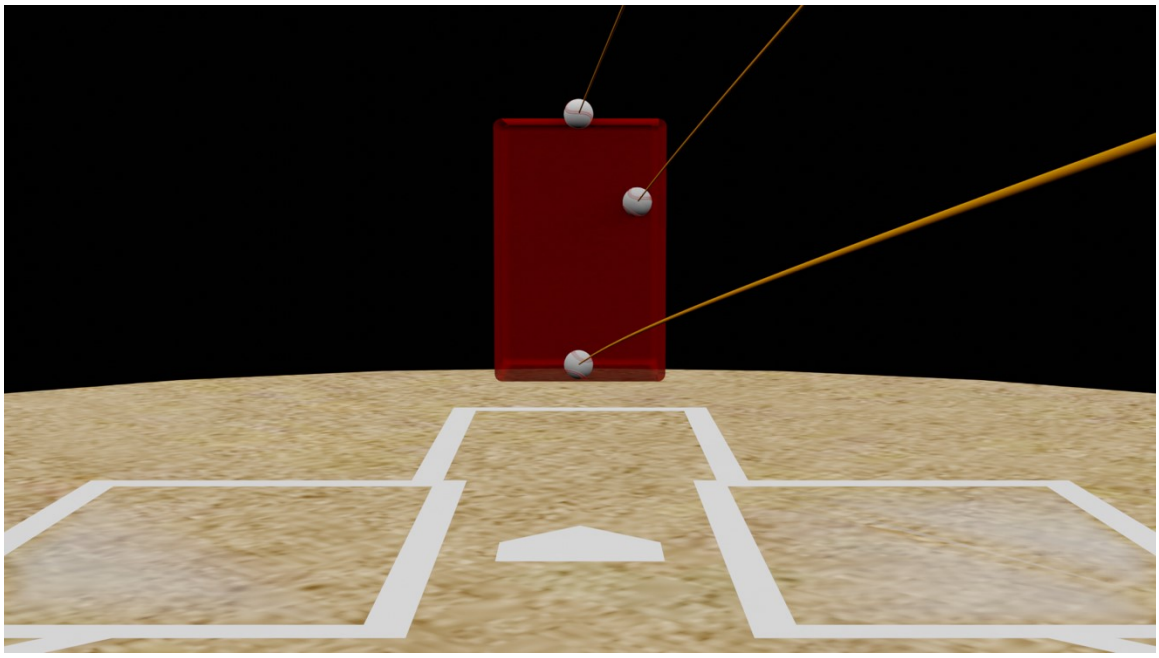

Figure 3-24. Final location of a four-seam baseball pitched with $\alpha = 0°$ (bottom), $\alpha = 45°$ (right), and $\alpha = 90°$ (top), when "aimed" at the middle of the strike zone

CHAPTER 4. RESULTS AND DISCUSSION – FLETTNER ROTORS

In this chapter, simulation results for flows past three-dimensional rotating cylinders are presented. In the first section, the results for cylinders with surface suction are reported for various spin ratios and suction ratios and are compared to rotating cylinders with no suction. In the following section, results for tapered cylinders are reported and compared to straight cylinders at varying spin ratios. Results for tapered cylinders are then used for an exploratory design study of a small drone which uses Flettner rotors for propulsion.

4.1 CYLINDERS WITH SURFACE SUCTION

Rotating cylinders with surface suction are simulated at $Re = 200$ for $\omega^* = 2.5$, 3.0, and 3.5. The suction ratio $\gamma = \frac{U_{suction}}{U_\infty}$ is investigated at 0.1, 0.2, and 0.5, and compared to the baseline case without suction. For the spin ratios investigated, the flow reaches a stationary state by 62.5 convective time units. Figure 4-1 shows the drag and lift in time for the sampled parameters. In all cases, increased suction velocity leads to a clear increase in lift, and the drag is nearly zero in all cases. For $\omega^* = 2.5$, increasing γ has the effects of increasing lift, decreasing drag, and shortening the time in the simulation to reach stationary state. Interestingly at $\omega^* = 3.5$, increased γ has the effect of slightly increasing drag and increasing the time to reach stationary state. Even for three-dimensional simulations, the flow has very little variation along the length of the cylinder (z-axis), so flows can be visualized using the z-vorticity component through the mid-plane of the cylinder (Figure 4-2).

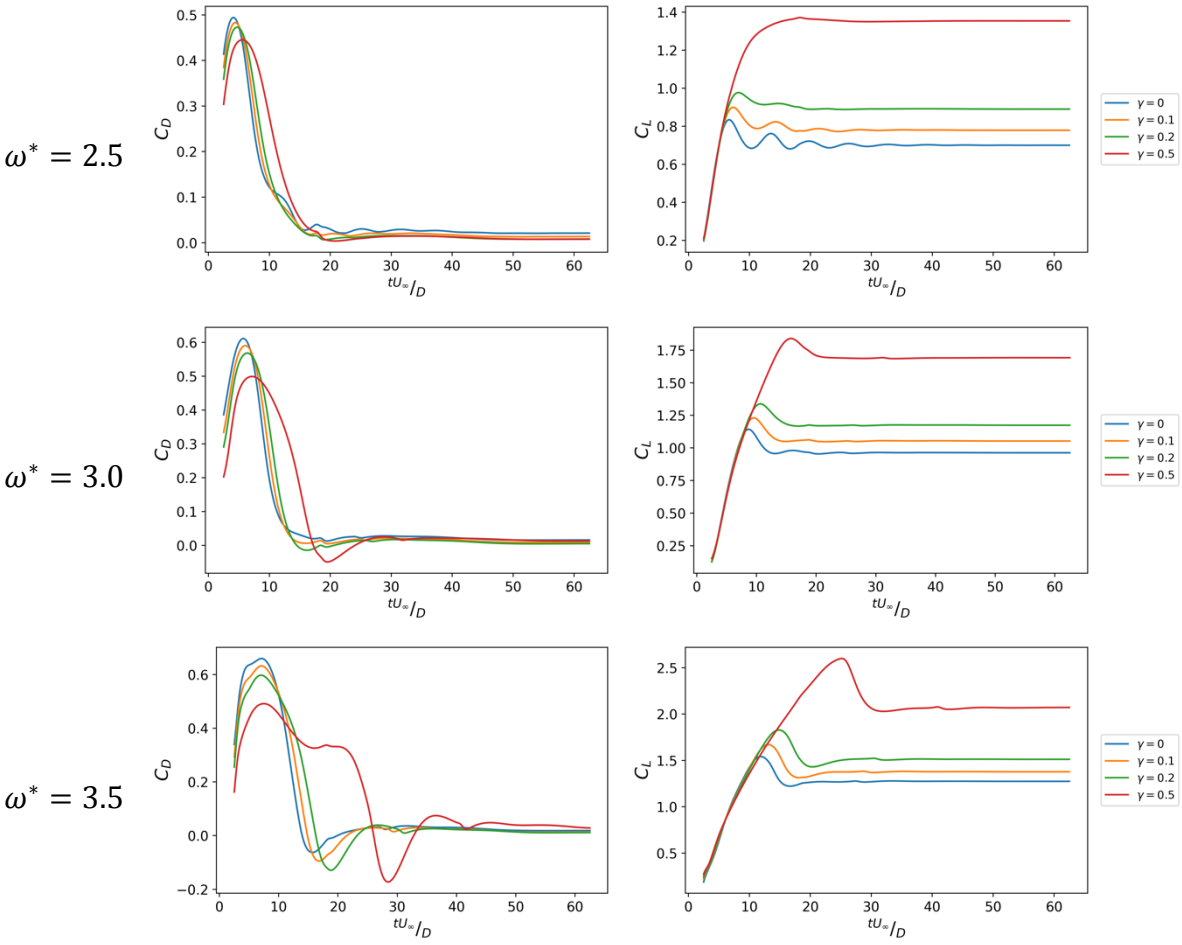

Figure 4-1. Time history of drag (left) and lift (right) for cylinders with suction at $Re = 200$

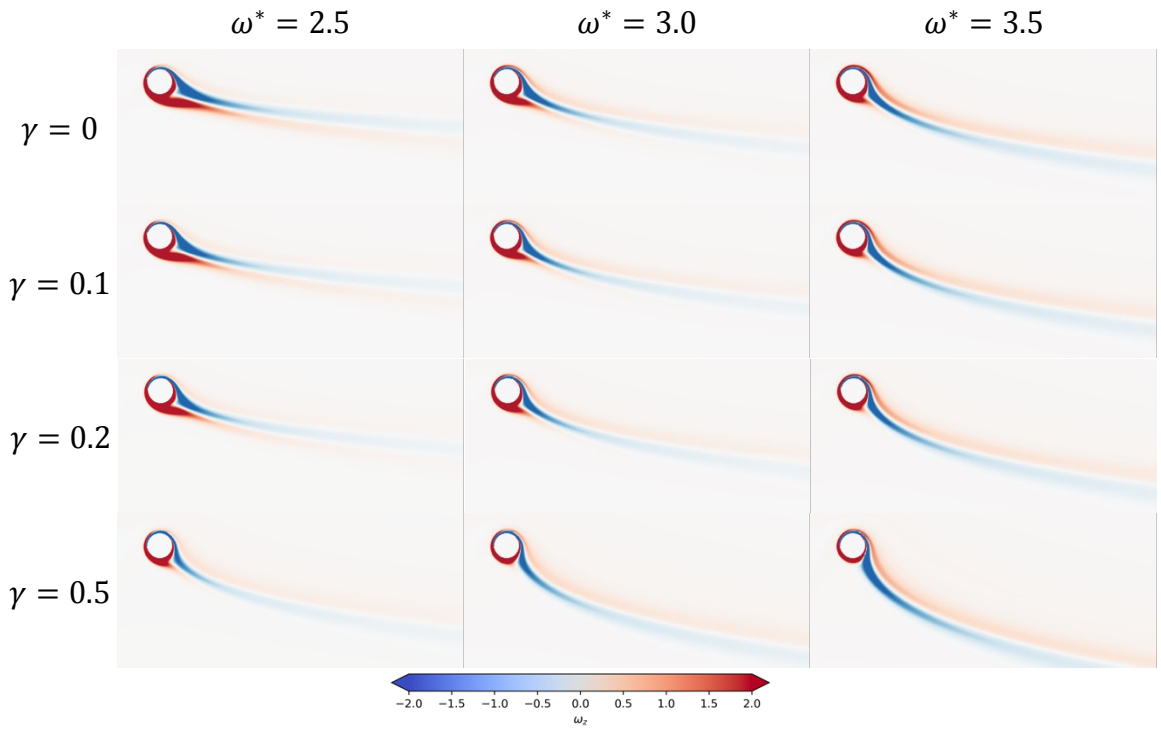

Figure 4-2. Vorticity contours for $\omega^* = 2.5 - 3.5$, $\gamma = 0 - 0.5$ at $Re = 200$

Increases in both ω^* and γ lead to a shrinking of the positive vorticity region near the stagnation, which is approximately 180° from the location of the suction zone. The suction assists the circulation produced by the rotation of the sphere, moving the stagnation point towards the bottom of the sphere and causing a more favorable pressure distribution for increased lift. Figure 4-3 shows comparisons of the lift-to-drag ratio and the percentage increase in lift due to suction. With increased γ, the optimal L/D is achieved at lower ω^* – at $\gamma = 0$, L/D increases with ω^*, while at $\gamma = 0.5$, L/D decreases with ω^*. For values of γ, the greatest percentage increase in lift is achieved at $\omega^* = 2.5$, with the lift nearly doubling for $\gamma = 0.5$. While the surface suction certainly indicates favorable aerodynamic performance as compared to a Flettner rotor with no suction, further design considerations would need to consider the power consumption trade-off

and feasibility when implementing a surface suction, especially for a suction velocity as high as 50% of the free-stream velocity.

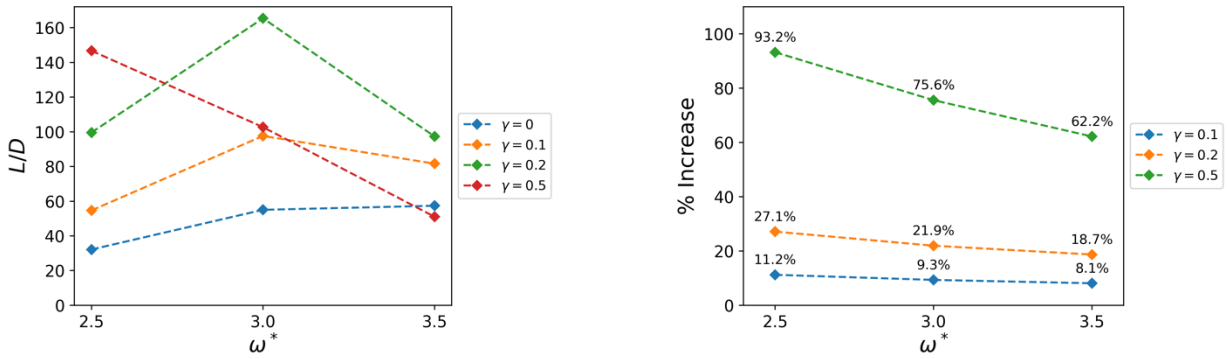

(a) (b)

Figure 4-3. (a) Lift-to-drag ratio for cylinder with various ω^* and γ and (b) percentage increase in drag over baseline case (no suction)

4.2 TAPERED CYLINDERS

In this section, simulations of rotating cylinders with different profiles in a shear flow are reported. Cylinders are simulated at $Re = \frac{\langle U_\infty \rangle D}{\nu} = 200$, with a slight modification in the Reynolds number definition to account for the non-uniform free-stream velocity. Simulations are performed at $\omega^* = \frac{\omega D}{2\langle U_\infty \rangle} = 2.0 - 4.0$, for two different cylinder geometries: a "straight" cylinder, and a "tapered" cylinder. The straight cylinder is the same geometry as simulated in the previous section, with a uniform cross-sectional area along the span of the cylinder. The tapered cylinder considered has a linearly varying diameter along the span, with an end diameter ratio of 2:1, and the mid-span diameter set equal to the straight cylinder diameter. The larger end of the tapered cylinder is set to the "fast" side of the domain, with the smaller end of the cylinder set to the "slow" side of the domain. The motivation for investigating this particular geometry is that, as opposed to in a

uniform inflow, the local $\omega^*(z)$ is not uniform on the cylinder surface in a shear inflow. Therefore, since $U_\infty(z)$ increases linearly along the span of the cylinder, a cylinder whose diameter also increases linearly along the span will have a more uniform local $\omega^*(z)$ profile, and possibly a more stable flow than a straight cylinder.

Figure 4-4 shows instantaneous flow structures for straight and tapered cylinders across the range of ω^* simulated. From this perspective, the fast end of the cylinder is located to the left and the slow end to the right. Both due to the non-uniform inflow velocity and the finite cylinder span, the flows are much more three-dimensional than in the surface suction simulations. At both ends of the cylinder, tip vortex-like structures are formed. At higher ω^*, the flow becomes increasingly unsteady for both cylinder geometries. At the slow end, the tip vortex is much more stable for the tapered cylinder as compared to the straight cylinder for all ω^*. At the fast end, the opposite is true, as the flow past the tapered cylinder is steady at lower ω^* but becomes unstable for higher ω^*, while the tip vortex remains steady for the straight cylinder.

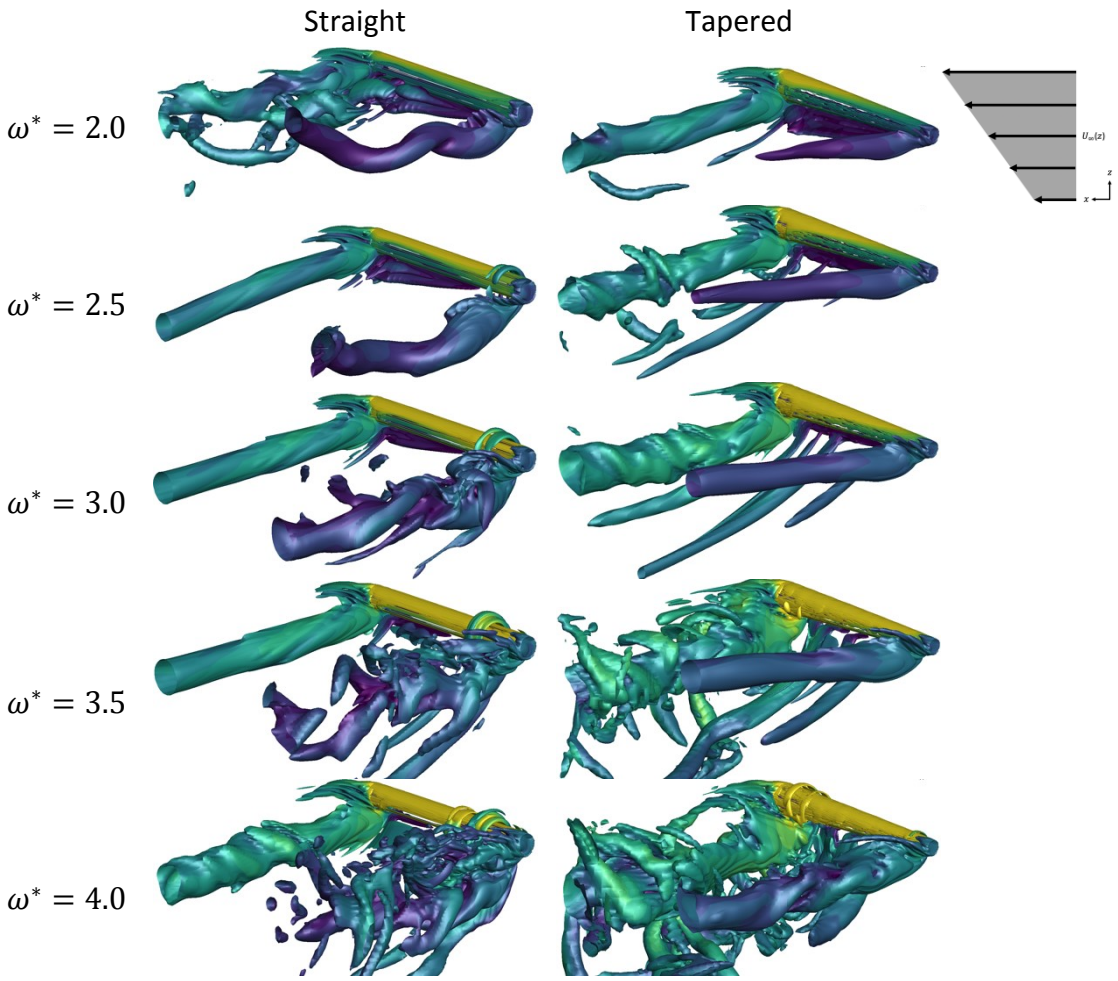

Figure 4-4. Isosurface plots of instantaneous flow structures for straight cylinders (left) and tapered cylinders (right) in shear flow, colored by $\overline{\boldsymbol{u}}$

Figures 4-5 and 4-6 show the time histories of lift and drag and the mean lift-to-drag ratios, respectively. Due to the finite cylinder span, the drag substantially increased from the infinite span surface suction simulations. The trends and overall behavior of the force coefficients are similar between the two cylinder geometries – with increased ω^*, both lift and drag increase for both cases. At $\omega^* = 3.5$ and 4.0, the forces become more unsteady in time compared to lower spin ratios, a similar trend to the flow structures seen in Figure 4-4. As the flow becomes more unsteady at higher ω^*, the lift-to-drag ratios decrease for both cylinder geometries. At lower ω^*, the tapered

cylinder has a slightly better performance than the straight cylinder, while above $\omega^* = 3.0$ the straight cylinder has a better lift-to-drag ratio. In both cases, $\omega^* = 2.0$ has the optimal lift-to-drag ratios – 3.53 for the straight cylinder, and 3.63 for the tapered cylinder.

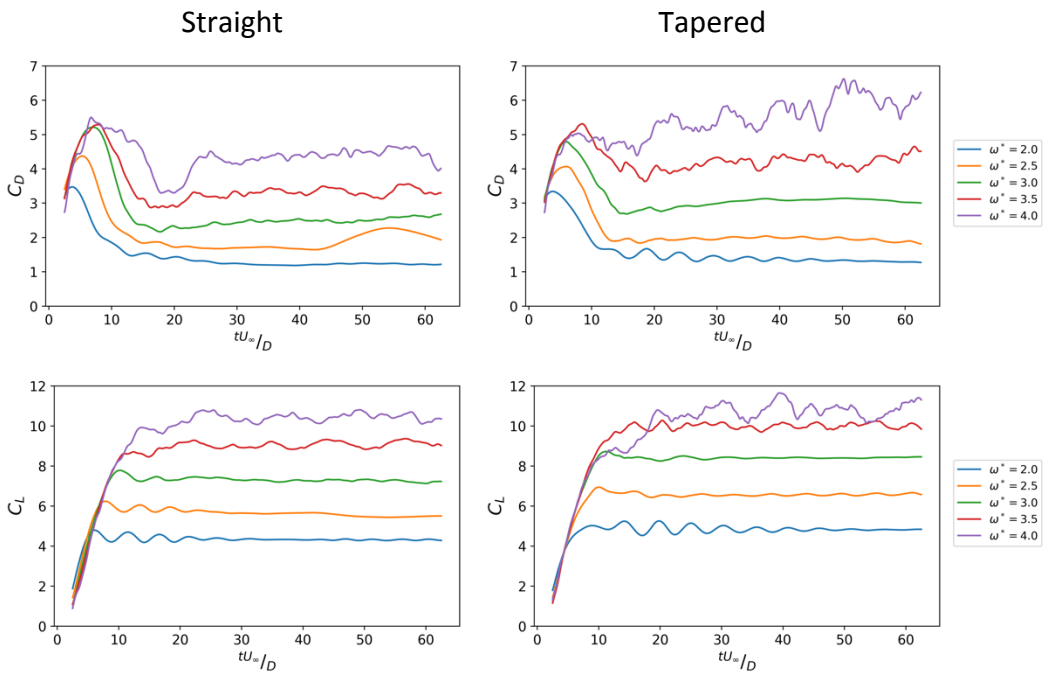

Figure 4-5. Time history of drag (left) and lift (right) for straight and tapered cylinders in shear flow at $Re = 200$

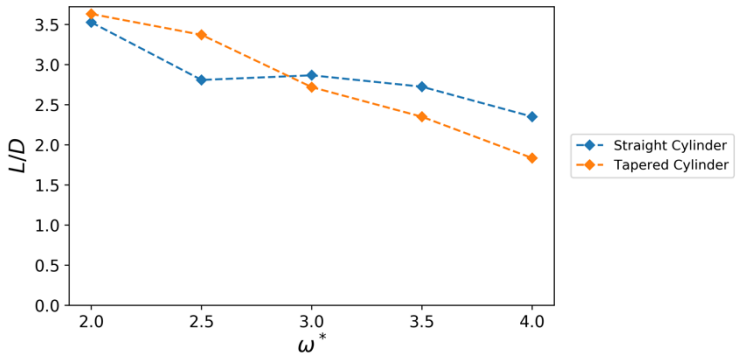

Figure 4-6. Lift-to-drag ratio for straight and tapered cylinders in shear flow at $Re = 200$

4.3 FLETTNER DRONE DESIGN STUDY

In this section, data from simulations in the previous section are used for a design study of a "Flettner drone" application. In this concept, a drone device is proposed which uses Flettner rotors in place of blades. Given that the cylinder in this setup would be rotating about a central pivot point, simulation data with a shear inflow boundary condition are more applicable than with a uniform inflow. The primary design considerations are the mechanical power required to obtain 55 lbf thrust (the maximum load allowed for a small unmanned aircraft in the United States, per FAA rule 14 CFR Part 107), and the loading noise. A simplified schematic of a Flettner drone is shown in Figure 4-7

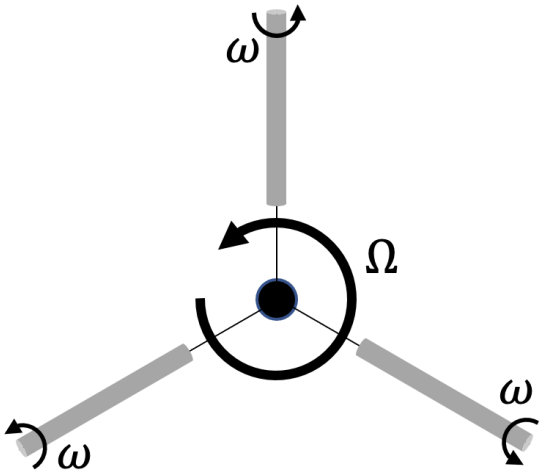

Figure 4-7: "Flettner drone" concept with cylinder rotating about a central point

For a drone with N rotors, the total thrust is obtained by $F_{Lift} = N\left(\frac{1}{2}\rho A C_L U^2\right)$, where ρ is the atmospheric density, A is the cross-section area, C_L is the lift (dependent on ω^*), and U is the free-stream velocity. With a variable free-stream velocity $U(z) = \Omega z$, the mean value $\langle U^2(z)\rangle = \omega^2\langle z^2\rangle$ is used instead. With the shear velocity profile specified in Section 2.4.2, $\langle z^2\rangle$ across the length of the cylinder becomes $\langle z^2\rangle = L^2$, where L is the length of the cylinder. With the cross-

sectional area $A = LD$, the total thrust then becomes $F_{Lift} = N\left(\frac{1}{2}\rho L^3 D C_L \Omega^2\right)$, and the drag is $F_{Drag} = N\left(\frac{1}{2}\rho L^3 D C_D \Omega^2\right)$, and the required Ω for a specified thrust can be obtained. Assuming the drag to be a point force at the middle of the cylinder where $z_{midpoint} \approx L$, the mechanical power can be estimated as $P = F_D L\Omega = N\left(\frac{1}{2}\rho L^4 D C_D \Omega^3\right)$. The loading noise generated from the cylinders rotating with angular velocity Ω can be estimated as $p_L' \sim F_D \frac{R\Omega^2}{4\pi r c^2}$, where p_L' is the loading noise, R is the drone radius, r is the distance to the observer, and c is the speed of sound. The noise level can then be estimated as $Noise \sim 20 \log\left(\frac{p_L'}{p_{ref}}\right) [dB\}$

In this sample calculation, a drone with $N = 12$ Flettner rotors is considered, with a rotor length of 20 cm and a rotor diameter of 2 cm, at atmospheric pressure, with noise calculated for an observed $1\ m$ away. Figure 4-8 shows the predicted loading noise for prescribed thrust levels for straight and tapered cylinders. In both cases, loading noise is approximately $85 - 90\ dB$ for $\omega^* = 2.0 - 4.0$. Considering the power requirements and noise at various ω^*, shown in Figure 4-9, the optimal spin ratio for minimizing power and noise is $\omega^* = 3.5$ for a straight cylinder, while the noise and power. For both cylinder geometries, the power requirement is approximately $3\ kW$.

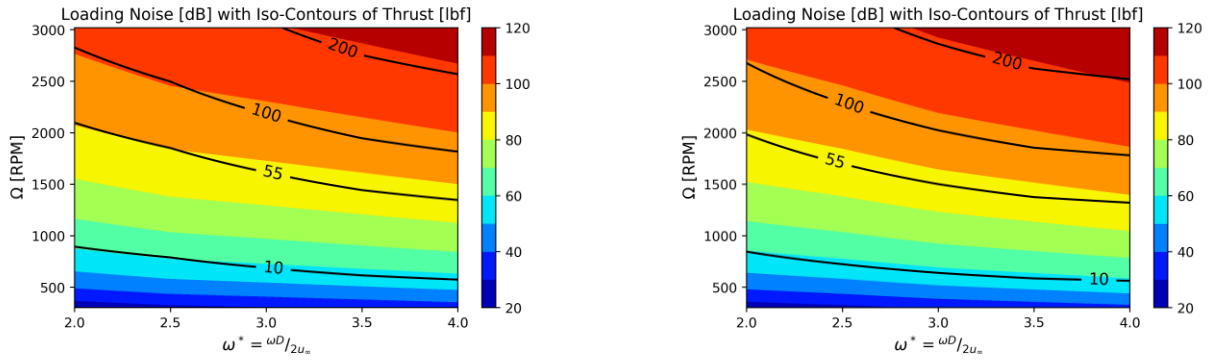

(a) (b)

Figure 4-8: Colors of noise [dB] with iso-lines of thrust [lbf] for (a) straight and (b) tapered cylinders at $\omega^* = 2.0 - 4.0$

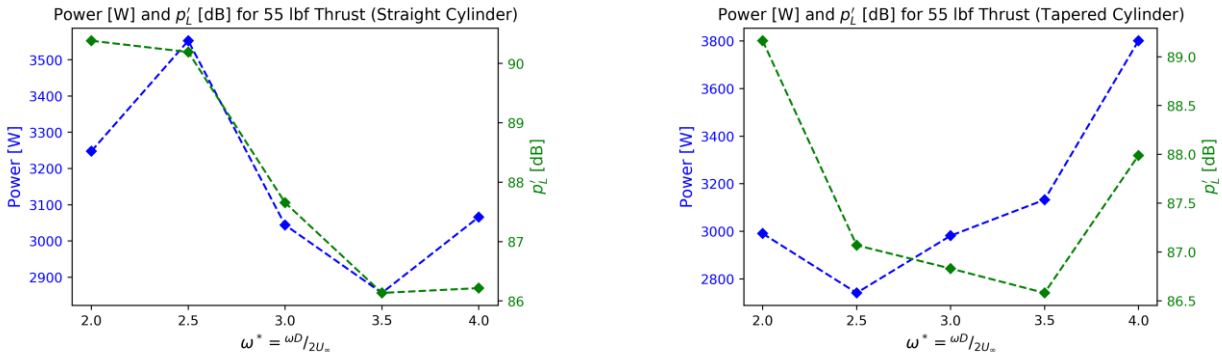

(a) (b)

Figure 4-9: Power requirements and loading noise at 55 lbf thrust for (a) straight and (b) tapered cylinders at $\omega^* = 2.0 - 4.0$

LIST OF REFERENCES

Albert, J., Bartroff, J., Blandford, R., Brooks, D., Derenski, J., Goldstein, L., … Smith, L. (2018). *Report of the Committee Studying Home Run Rates in Major League Baseball*.

Anderson, D. A., Tannehill, J. C., & Pletcher, R. H. (1984). Computational fluid mechanics and heat transfer. https://doi.org/10.2307/2008017

Balasubramanian, S., Haan, F. L., Szewczyk, A. A., & Skop, R. A. (2001). An experimental investigation of the vortex-excited vibrations of pivoted tapered circular cylinders in uniform and shear flow. *Journal of Wind Engineering and Industrial Aerodynamics*. https://doi.org/10.1016/S0167-6105(00)00093-3

Benton, E. R. (1965). Laminar boundary layer on an impulsively started rotating sphere. *Journal of Fluid Mechanics*. https://doi.org/10.1017/S002211206500157X

Bozkurttas, M., Dong, H., Seshadri, V., Mittal, R., & Najjar, F. (2005). Towards numerical simulation of flapping foils on fixed cartesian grids. In *43rd AIAA Aerospace Sciences Meeting and Exhibit - Meeting Papers*. https://doi.org/10.2514/6.2005-79

Briggs, L. J. (1959). Effect of Spin and Speed on the Lateral Deflection (Curve) of a Baseball; and the Magnus Effect for Smooth Spheres. *American Journal of Physics*. https://doi.org/10.1119/1.1934921

Burns, K. (1994). *Baseball*.

Chong, M. S., Perry, A. E., & Cantwell, B. J. (1990). A general classification of three-dimensional flow fields. *Physics of Fluids A*. https://doi.org/10.1063/1.857730

Eiffel, G. (1912). Eiffel G. Sur la résistance des sphères dans l'air en mouvement.

Felten, F. N., & Lund, T. S. (2006). Kinetic energy conservation issues associated with the collocated mesh scheme for incompressible flow. *Journal of Computational Physics*. https://doi.org/10.1016/j.jcp.2005.11.009

Fransson, J. H. M., Konieczny, P., & Alfredsson, P. H. (2004). Flow around a porous cylinder subject to continuous suction or blowing. *Journal of Fluids and Structures*. https://doi.org/10.1016/j.jfluidstructs.2004.06.005

Gaster, M. (1969). Vortex shedding from slender cones at low Reynolds numbers. *Journal of Fluid Mechanics*. https://doi.org/10.1017/S0022112069000346

Gerrard, J. H. (1997). Flow around Circular Cylinders; Volume 1. Fundamentals. By M. M. Zdravkovich. Oxford Science Publications, 1997. 672 *Journal of Fluid Mechanics*. https://doi.org/10.1017/s0022112097227291

Giacobello, M., Ooi, A., & Balachandar, S. (2009). Wake structure of a transversely rotating sphere at moderate Reynolds numbers. *Journal of Fluid Mechanics*. https://doi.org/10.1017/S0022112008004655

Hoskins, N. E. (1955). The laminar boundary layer on a rotating sphere.

Hurley, D. G., & Thwaites, B. (1955). *An experimental investigation of the boundary layer on a porous circular cylinder*. *Aeronautical Research Council Reports and Memoranda*.

Kang, S. (2006). Uniform-shear flow over a circular cylinder at low Reynolds numbers. *Journal of Fluids and Structures*. https://doi.org/10.1016/j.jfluidstructs.2006.02.003

Kim, D. (2009). Laminar flow past a sphere rotating in the transverse direction. *Journal of Mechanical Science and Technology*. https://doi.org/10.1007/s12206-008-1001-9

Kim, D., & Choi, H. (2002). Laminar flow past a sphere rotating in the streamwise direction. *Journal of Fluid Mechanics*. https://doi.org/10.1017/S0022112002008509

Liu, Q., & Prosperetti, A. (2010). Wall effects on a rotating sphere. *Journal of Fluid Mechanics*. https://doi.org/10.1017/S002211201000128X

Magnus, G. (1853). Über die Abweichung der Geschosse. *Abhandlungen Der Königlichen Akademie Der Wissenschaften Zu Berlin*.

Mittal, R., Dong, H., Bozkurttas, M., Najjar, F. M., Vargas, A., & von Loebbecke, A. (2008). A versatile sharp interface immersed boundary method for incompressible flows with complex boundaries. *Journal of Computational Physics*. https://doi.org/10.1016/j.jcp.2008.01.028

Mittal, R., & Iaccarino, G. (2005). Immersed boundary methods. *Annual Review of Fluid Mechanics*. https://doi.org/10.1146/annurev.fluid.37.061903.175743

Mittal, S., & Raghuvanshi, A. (2001). Control of vortex shedding behind circular cylinder for flows at low Reynolds numbers. *International Journal for Numerical Methods in Fluids*. https://doi.org/10.1002/1097-0363(20010228)35:4<421::AID-FLD100>3.0.CO;2-M

Mittal, S., & Kumar, B. (2003). Flow past a rotating cylinder. *Journal of Fluid Mechanics*. https://doi.org/10.1017/S0022112002002938

Nathan, A. M. (2008). The effect of spin on the flight of a baseball. *American Journal of Physics*, *76*(2). https://doi.org/10.1119/1.2805242

Nathan, A. M., Hopkins, J., Chong, L., & Kaczmarski, H. (2006). The effect of spin on the flight of a baseball. In *The Engineering of Sport 6*. https://doi.org/10.1007/978-0-387-46050-5_5

Newton, I. (1671). A Letter of Mr. Isaac Newton … containing his New Theory about Light and Colors. *Philosophical Transactions (1665-1678)*.

Neyer, R., & James, B. (2004). *The Neyer/James Guide to Pitchers*. Simon & Schuster.

Pallis, J., & Mehta, R. (2002). Aerodynamics and hydrodynamics in sports. *The Engineering of Sport*.

Papangelou, A. (1992). Vortex shedding from slender cones at low reynolds numbers. *Journal of Fluid Mechanics*. https://doi.org/10.1017/S0022112092002386

Poon, E. K. W., Iaccarino, G., Ooi, A. S. H., & Giacobello, M. (2009). Numerical studies of high Reynolds number flow past a stationary and rotating sphere. *Proceedings of the 7th International Conference on CFD in the Minerals and Process Industries*.

Poon, E. K. W., Ooi, A. S. H., Giacobello, M., & Cohen, R. C. Z. (2010). Laminar flow structures from a rotating sphere: Effect of rotating axis angle. *International Journal of Heat and Fluid Flow*. https://doi.org/10.1016/j.ijheatfluidflow.2010.04.005

Poon, E. K. W., Ooi, A. S. H., Giacobello, M., Iaccarino, G., & Chung, D. (2014). Flow past a transversely rotating sphere at Reynolds numbers above the laminar regime. *Journal of Fluid Mechanics*. https://doi.org/10.1017/jfm.2014.570

Poon, K. W., Ooi, A., Giacobello, M., Peralta, C., & Melatos, A. (2007). Numerical simulation of flow past a stationary and rotating sphere. In *Proceedings of the 16th Australasian Fluid Mechanics Conference, 16AFMC*.

Raman, V. M. (1984). Numerical prediction of a laminar boundary layer flow on a rotating sphere. *Computer Methods in Applied Mechanics and Engineering*. https://doi.org/10.1016/0045-7825(84)90093-8

Ramsay, J., Sellier, M., & Ho, W. H. (2020). Non-uniform suction control of flow around a circular cylinder. *International Journal of Heat and Fluid Flow*. https://doi.org/10.1016/j.ijheatfluidflow.2020.108559

Rex, A. F. (1985). The effect of spin on the flight of batted baseballs. *American Journal of Physics*. https://doi.org/10.1119/1.14034

Rubinow, S. I., & Keller, J. B. (1961). The transverse force on a spinning sphere moving in a viscous fluid. *Journal of Fluid Mechanics*. https://doi.org/10.1017/S0022112061000640

Schlichting, H., & Gersten, K. (2016). *Boundary-Layer Theory*. *Boundary-Layer Theory*. https://doi.org/10.1007/978-3-662-52919-5

Seifert, J. (2012). A review of the Magnus effect in aeronautics. *Progress in Aerospace Sciences*. https://doi.org/10.1016/j.paerosci.2012.07.001

Seo, J. H., & Mittal, R. (2011). A sharp-interface immersed boundary method with improved mass conservation and reduced spurious pressure oscillations. *Journal of Computational Physics*. https://doi.org/10.1016/j.jcp.2011.06.003

Smith, A. W., & Smith, B. L. (2020). Using baseball seams to alter a pitch direction: The seam shifted wake. *Proceedings of the Institution of Mechanical Engineers, Part P: Journal of Sports Engineering and Technology*. https://doi.org/10.1177/1754337120961609

Sturek, W. B., Dwyer, H. A., Kayser, L. D., Nietubicz, C. J., Reklis, R. P., & Opalka, K. O. (1978). Computations of magnus effects for a yawed, spinning body of revolution. *AIAA Journal*. https://doi.org/10.2514/3.7566

van Kan, J. (1986). A Second-Order Accurate Pressure-Correction Scheme for Viscous Incompressible Flow. *SIAM Journal on Scientific and Statistical Computing*. https://doi.org/10.1137/0907059

Verwiebe, F. L. (1942). Does a Baseball Curve? *American Journal of Physics1*, *10*(119).

Watts, R. G., & Ferrer, R. (1987). The lateral force on a spinning sphere: Aerodynamics of a curveball. *American Journal of Physics*. https://doi.org/10.1119/1.14969

Watts, R. G., & Sawyer, E. (1975). Aerodynamics of a knuckleball. *American Journal of Physics*. https://doi.org/10.1119/1.10020

Wu, X., Wang, Q., Luo, Z., Fang, M., & Cen, K. (2008). Experimental study of particle rotation characteristics with high-speed digital imaging system. *Powder Technology*. https://doi.org/10.1016/j.powtec.2007.04.007

Ye, T., Mittal, R., Udaykumar, H. S., & Shyy, W. (1999). An Accurate Cartesian Grid Method for Viscous Incompressible Flows with Complex Immersed Boundaries. *Journal of Computational Physics*. https://doi.org/10.1006/jcph.1999.6356

Zang, Y. (1994). A non-staggered grid, fractional step method for time-dependent incompressible navier-stokes equations in curvilinear coordinates. *Journal of Computational Physics*. https://doi.org/10.1006/jcph.1994.1146

Ziegel, E., Press, W., Flannery, B., Teukolsky, S., & Vetterling, W. (1987). Numerical Recipes: The Art of Scientific Computing. *Technometrics*. https://doi.org/10.2307/1269484

BIOGRAPHICAL STATEMENT

John Scheffey was born in Federal Way, Washington. John completed his undergraduate study at Northeastern University in Boston, Massachusetts, where he majored in mechanical engineering with minors in mathematics and physics. During his time at Northeastern University, John was a pitcher on the men's varsity baseball team. After receiving his Bachelor of Science in May 2019, John entered the mechanical engineering graduate program at John Hopkins University in Baltimore, Maryland in August 2019. John is currently in his second year of graduate study, where he is a research assistant in the Flow Physics and Computation Lab with Dr. Rajat Mittal. John's research interests include sports aerodynamics, biomechanics, biological flows, and sports physiology.